DTIC FILE COPY

(2)

SSS-TR-90-11536

GL-TR-90-0126

AN ANALYSIS OF THE EFFECTS OF SPALL ON REGIONAL AND TELESEISMIC WAVEFORMS USING TWO-DIMENSIONAL NUMERICAL MODELING OF UNDERGROUND EXPLOSIONS

AD-A226 921

T. G. Barker
S. M. Day
K. L. McLaughlin
B. Shkoller
J. L. Stevens

DTIC
ELECTE
SEP 25 1990
S D
D

S-CUBED
A Division of Maxwell Laboratories, Inc.
P.O. Box 1620
La Jolla, CA 92038-1620

May 1990

Scientific Report No. 1

Approved for Public Release; Distribution Unlimited

GEOPHYSICS LABORATORY
UNITED STATES AIR FORCE
AIR FORCE SYSTEMS COMMAND
HANSCOM AIR FORCE BASE, MA 01731-5000

90 09 24 010

SPONSORED BY
Defense Advanced Research Projects Agency
Nuclear Monitoring Research Office
ARPA ORDER NO 5307

MONITORED BY
Geophysics Laboratory
F19628-89-C-0043

The views and conclusions contained in this document are those of the authors and should not be interpreted as representing the official policies, either expressed or implied, of the Defense Advanced Research Projects Agency or the U.S. Government.

This technical report has been reviewed and is approved for publication.

JAMES F. LEWKOWICZ
Contract Manager
Solid Earth Geophysics Branch
Earth Sciences Division

JAMES F. LEWKOWICZ
Branch Chief
Solid Earth Geophysics Branch
Earth Sciences Division

FOR THE COMMANDER

DONALD H. ECKHARDT, Director
Earth Sciences Division

This report has been reviewed by the ESD Public Affairs Office (PA) and is releasable to the National Technical Information Service (NTIS).

Qualified requestors may obtain additional copies from the Defense Technical Information Center. All others should apply to the National Technical Information Service.

If your address has changed, or if you wish to be removed from the mailing list, or if the addressee is no longer employed by your organization, please notify GL/IMA, Hanscom AFB, MA 01731-5000. This will assist us in maintaining a current mailing list.

Do not return copies of this report unless contractual obligations or notices on a specific document requires that it be returned.

REPORT DOCUMENTATION PAGE

Form Approved OMB No. 0704-0188

Public reporting burden for this collection of information is estimated to average 1 hour per response, including the time for reviewing instructions, searching existing data sources gathering and maintaining the data needed, and completing and reviewing the collection of information. Send comments regarding this burden estimate or any other aspect of this collection of information, including suggestions for reducing this burden, to Washington Headquarters Services, Directorate for Information Operations and Reports, 1215 Jefferson Davis Highway, Suite 1204, Arlington, VA 22202-4302, and to the Office of Management and Budget, Paperwork Reduction Project (0704-0188), Washington, DC 20503.

1. AGENCY USE ONLY *(Leave blank)*	2. REPORT DATE	3. REPORT TYPE AND DATES COVERED
	May 1990	Scientific Report #1 03/29/89-03/29/90

4. TITLE AND SUBTITLE
AN ANALYSIS OF THE EFFECTS OF SPALL ON REGIONAL AND TELESEISMIC WAVEFORMS USING TWO-DIMENSIONAL NUMERICAL MODELING OF UNDERGROUND EXPLOSIONS

5. FUNDING NUMBERS
F19628-89-C-0043
PE 62714E
PR 9A10
TA 0A
WU BG

6. AUTHOR(S)
Barker, T. G., Day, S. M., McLaughlin, K. L., Shkoller, B., Stevens, J. L.

7. PERFORMING ORGANIZATION NAME(S) AND ADDRESS(ES)
S-CUBED, A Division of Maxwell Laboratories, Inc.
P.O. Box 1620
La Jolla, CA 92038-1620

8. PERFORMING ORGANIZATION REPORT NUMBER
SSS-TR-90-11536

9. SPONSORING/MONITORING AGENCY NAME(S) AND ADDRESS(ES)
Geophysics Laboratory
Hanscom Air Force Base
Massachusetts 01731-5000
Contract Manager: James Lewkowicz/LWH

10. SPONSORING/MONITORING AGENCY REPORT NUMBER
GL-TR-90-0126

11. SUPPLEMENTARY NOTES

12a. DISTRIBUTION/AVAILABILITY STATEMENT
Approved for Public Release; Distribution Unlimited

12b. DISTRIBUTION CODE

13. ABSTRACT *(Maximum 200 words)*

A simple, physical model for spall is developed by comparing the waveforms from two-dimensional explosion simulations with the waveforms generated by a one-dimensional explosion plus a shallow tension crack in the same layered medium. The tension crack is parameterized by its radius, depth, and a distribution of takeoff velocities over its surface. This model accurately reproduces the P-waves from the two-dimensional simulations. The parameters for the spall model are consistent with the limited set of near-field observations of spall. P-waves generated by the tension crack have a narrow band spectrum proportional to ω^2 at low frequencies and $\omega^{-5/2}$ at high frequencies.

The spall model is used to generate complete regional seismograms for an explosion plus spall source. In high velocity structures, a spherically symmetric explosion source is a very poor generator of Lg while the tension crack is a good generator of Lg, so the Lg generated by spall completely dominates the regional Lg signal. In a structure with low

(Over)

14. SUBJECT TERMS
Spall, Seismic Waveforms, Regional Waveforms, Explosion, Finite Difference, Teleseismic Waveforms

15. NUMBER OF PAGES
98

16. PRICE CODE

17. SECURITY CLASSIFICATION OF REPORT	18. SECURITY CLASSIFICATION OF THIS PAGE	19. SECURITY CLASSIFICATION OF ABSTRACT	20. LIMITATION OF ABSTRACT
UNCLASSIFIED	UNCLASSIFIED	UNCLASSIFIED	SAR

CLASSIFIED BY:

DECLASSIFY ON:

13. (Continued)

velocities at the source, Lg generation by an explosion is comparable to the generation of Lg by spall. Regional seismic signals of the NTS explosions Duryea and Buteo, two explosions at the same location with very different scaled depths of burial, show no measurable difference other than that due to yield scaling.

Two additional areas of research are currently in progress under this contract: implementation of scale-dependent damage mechanics in S-CUBED nonlinear finite difference codes; and a finite difference simulation of the Salmon experiment.

TABLE OF CONTENTS

SECTION		PAGE
I	Introduction	1
II	A Simple Physical Model for Spall from Nuclear Explosions Based Upon Two-Dimensional Nonlinear Numerical Simulations	6
III	Implications of Explosion Generated Spall Models: Regional Seismic Signals	31
IV	Analysis of Pg and Lg Excitation by Axisymmetric Sources in Layered Anelastic Crustal Models	40
V	An Analysis of Two Co-Located NTS Events with Different Scaled Depths of Burial	62
VI	Research in Progress	72
VII	References	78

DTIC COPY

Accession For
NTIS
DTIC
Unannounced
Justification
By
Distribution/
Availability Codes
Dist
A-1

LIST OF ILLUSTRATIONS

FIGURE		PAGE
2.1	The tension crack model for spall	9
2.2	Schematic drawing of the detachment acceleration, which is proportional to the P-wave displacement for constant detachment velocity	11
2.3	Spectrum of far-field P-waves from the tension crack model	13
2.4	Comparison of the far-field P-waves from the 1-D (solid lines) and 2-D (dashed lines) Shagan River simulations for four depths of burial at a take-off angle of 10°	16
2.5	Comparison of the far-field SV-waves from the 1-D (solid lines) and 2-D (dashed lines) Shagan River simulations for four depths of burial at a take-off angle of 10°	17
2.6	Comparison of the 2D-1D P-waves solutions from the Shagan River simulation with the tension crack P-waves	20
2.7	Comparison of the 2D-1D P-waves solutions from the Shagan River simulation with the tension crack SV-waves	22
2.8	Comparison of the far-field P-waves solutions from the 1-D (solid lines) and 2-D (dashed lines) Pahute Mesa simulations for three depths of burial at a take-off angle of 3.3°	24
2.9	Comparison of the differential 2D-1D P-waves solutions from the Pahute Mesa simulations with the tension crack P-waves	26
3.1	The axisymmetric spall above the explosion is modeled as a circular horizontal tension crack that opens and closes in the vertical direction	33

LIST OF ILLUSTRATIONS (Continued)

FIGURE		PAGE
3.2	The equivalent spall source (for source depth of 680 m) for four different apparent phase velocities corresponding to teleseismic P, Pn, Pg and Lg	35
3.3	Spectra of the time series of Figure 3.2	36
3.4	Synthetic Lg and Pg waveforms at a distance of 300 km for the 680 meter depth of burial 125 KT Shagan River explosion simulation	37
3.5	Spectra of the time series in Figure 3.4	38
4.1	Explosion Green's functions (0-5 Hz) at a distance of 300 km for source depths of 100 to 1300 m	45
4.2	Theoretical LgPg ratio as a function of frequency and depth for a point explosion source at Δ = 300 km in a high velocity structure (Stevens, 1986)	47
4.3	Tension crack Green's functions (0-5 Hz) at a distance of 300 km for source depths of 100 to 1300 m	48
4.4	Explosion Green's functions (0-4 Hz) at a distance of 256 km for a suite of different crustal structures	50
4.5	CLVD Green's functions (0-4 Hz) at a distance of 256 km for a suite of different crustal structures	51
4.6	Explosion and CLVD Green's functions (0-4 Hz) at a distance of 320 km in the BR3 model	53
5.1	Duryea and Buteo recorded on the short period vertical channel at LRSM station KN-UT (Kanab, Utah)	65

LIST OF ILLUSTRATIONS (Continued)

FIGURE		PAGE
5.2	Ratios of bandpass filtered KN-UT records of Duryea and Buteo	66
5.3	Broadband velocity (m/s) synthetics from 0 to 2 Hz for step function sources with moment 10^{16} Nt-m	68
5.4	Lg/Pg ratios for a vertical receiver distance of 320 km as a function of frequency for three Green's functions; an explosion at 550 meter depth, an explosion at 250 meter depth	70
6.1	Model used for two-dimensional axisymmetric modeling of the Salmon explosion	76
6.2	Vertical seismogram at a distance of 16 km generated by analytic continuation of the finite difference calculation (bottom) seismogram for an explosion at a depth of 850 m (middle), and seismogram for a tensile crack at a depth of 50 m (top)	77

Section I

Introduction and Summary

In this report, we examine the effect of spall on regional and teleseismic waveforms using two-dimensional nonlinear numerical simulations of explosions. Each of the following sections covers a different topic related to this theme. Sections II and III are summaries of material that will be described in more detail in scientific reports which are now in preparation.

In Section II, we develop a simple, physical model for spall by comparing the complete two-dimensional waveform with the waveform generated by a one-dimensional explosion plus a shallow tension crack in the same layered medium. This is an extension to higher frequencies of the spall model derived by Day, *et al.* (1983). The waveform for a one-dimensional explosion is subtracted from the waveform for the two-dimensional simulation, and the residual, which contains all of the complex free-surface interactions, is interpreted as the waveform generated by the tension crack. The tension crack is parameterized by its radius, depth, and a distribution of takeoff velocities over its surface.

We find that the P-waves generated by the two-dimensional simulation are modeled very well by the simple tension crack plus explosion model. The resulting parameters for the spall model are consistent with the limited set of near-field observations of spall. The peak spall velocity is found to be much higher for underburied explosions than for normal or overburied explosions The spall depth decreases, but only slowly, as the explosion depth decreases. The

model underestimates the shear waves generated in the two-dimensional calculations, indicating that the source of shear waves is more complex than the simple explosion plus tension crack model.

The spall model is found to have a narrowband spectrum proportional to ω^2 at low frequencies and $\omega^{-5/2}$ at high frequencies. The spall spectrum is peaked at a frequency inversely proportional to the spall dwell time. A typical range for the peak frequency is from 0.5 to 5 Hz, which puts it in the middle of the frequency range where short period magnitudes are commonly measured.

In Section III, we use the model developed in Section II to generate regional seismograms for an explosion plus spall source. The source function derived from the spall model varies as a function of takeoff angle, or equivalent phase velocity, so the effective source functions are different for each regional phase. In particular, the lower the phase velocity, the more narrowband the spall source, so the Lg generated by the spall source is significantly more narrowband than the Pg, Pn, or teleseismic P-waves.

In high velocity structures, such as the model we used for the simulation of Shagan River area explosions, a spherically symmetric explosion source is a very poor generator of Lg. In contrast, the tension crack is a good generator of Lg, so the Lg generated by spall completely dominates the regional Lg synthetic. For a 125 kiloton simulation, we estimate an m_b(Lg) of 6.2 for the spall source and only 4.9 for the explosion source. The regional phases Pn and Pg, on the other hand, are comparable in amplitude for the spall and explosion sources. This is expected since the spall signal has the effect of partially

canceling the elastic pP signal and replacing it with a delayed and lower frequency phase.

In Section IV, we examine the effect of variations in earth structure on the generation of Lg by explosion and spall sources. This study was motivated by the results of Section III; in particular by the need to assess the robustness of the rather surprising conclusion that nearly all of the Lg synthetic for an explosion is due to spall. This result was tested by generating synthetic regional seismograms in a set of earth models derived by several authors for Eastern Kazakhstan near the Shagan River test site. The result was found to be independent of any of these structures. The characteristic of these structures that is responsible for this effect is a high source region P-wave speed, in excess of the Lg phase velocity. Under this condition, explosion Lg can be thought of as being generated by S*, a nongeometric arrival caused by the curvature of the wavefront. Since this phase decays exponentially with source depth, it is a very weak generator of Lg, and the resulting Lg will be swamped by the Lg from spall or any other deviatoric part of the source.

In contrast, for a structure with low velocities at the source, Lg generation by an explosion source is comparable to the generation of Lg by the spall source. The Lg phase generated by the spall or CLVD source is more complex than the Lg phase generated by the point explosion source; however, the peak amplitudes are similar, and Lg/Pg peak amplitude ratios are approximately equal.

It can be concluded from the results of Sections III and IV that a point explosion source is an unrealistic model for the generation of Lg for high velocity structures. Some physical effect must break the spherical symmetry of the source in order to generate the observed Lg amplitudes. Spall is one mechanism that breaks the spherical symmetry at a level sufficient to match the data. Other mechanisms, such as near source scattering, may also generate enough Lg to explain the data (see Section VI).

In Section V, we examine the regional seismic signals of the NTS explosions Duryea and Buteo. The significance of these explosions is that they are at the same location, but with very different scaled depths of burial. Duryea was at normal scaled depth, while Buteo was significantly overburied. Since spall should be greater for a shallow source than for a deep source, a comparison of these two explosions provides an opportunity to see if the generation of Lg is related to the amount of spall. Analysis of the data shows that there is no measurable difference between the regional signals from these two signals other than that due to standard yield scaling, so the difference in spall does not appear to have resulted in a difference in Lg. Unfortunately, since these explosions took place in a low velocity structure, where Lg/Pg ratios are expected to be similar for explosion and spall sources, it is not possible to separate the spall source from the explosion source in the data. A similar comparison in a high velocity structure would be definitive; however, no opportunity for such a comparison exists at present.

In Section VI, we summarize some of the additional research that is in progress under this contract. One important area of research is the implementation of damage mechanics, as developed by Sammis and Ashby, in S-CUBED nonlinear finite difference codes. The significance of this damage model is that it is scale dependent, and may be able to explain observed strength differences between laboratory and *in situ* rock. A second area of research is the effect of scattering on Lg. To this end, we are performing a finite difference simulation of the Salmon experiment, using a realistic model of the highly nonuniform structure near this explosion.

Section II

A Simple Physical Model for Spall from Nuclear Explosions Based Upon Two-Dimensional Nonlinear Numerical Simulations

Introduction

Several models have been proposed for the spall process that accompanies most nuclear explosions. The models are very difficult to validate directly because (1) the features of the process that can be measured, such as vertical motion at the surface, are observed at only a few locations above the shot, and (2) there are few observations of features such as the depth and area of the spall zone and the distribution of motions within the zone. Two-dimensional nonlinear simulations of the explosion, which include the physics of the free-surface interactions, provide an opportunity to examine spall, and to find simple models to represent it. In this section, we describe the work by Barker and Day (1990), who present a linear model for the spall process and find its parameters by comparing with the seismic waves from explosion simulations.

Using a form of the elastodynamic representation theorem, we have calculated the short-period body waves emanating from the source zone of the numerical simulations. The implications for teleseismic magnitude measurements were discussed in Day, *et al.* (1986) and McLaughlin, *et al.* (1988). By comparing these P and SV wavefields with one-dimensional nonlinear calculations (which do not include the nonlinear effects of the free-surface), we can isolate that part of the wave field due to the nonlinear interaction with the free-

surface. We find that a simple tension crack with an opening that propagates with the pP arrival from the explosion fits P-waves from simulations of both Pahute Mesa and Shagan River tests. However, the model which fits the P-wave radiation generates SV-waves that are too small, which indicates that there are additional sources of shear waves in the finite difference simulations.

The tension crack model, proposed in its original form by Day, *et al.* (1983), is a physical model whose parameters can be compared directly to field observations. The parameters of the model are spall depth and area, detachment velocity, and momentum. The parameters inferred from the simulations are consistent with published estimates of these values. The time dependence of the far-field waveforms is a natural consequence of the model and requires no *ad hoc* choice of time history to include the effects of source finiteness, the importance of which has been pointed out by Stump (1985). Although there is a trade-off between the parameters of the model, the amplitudes and waveforms from the two-dimensional (2-D) simulations tightly constrain the set of parameters which fit the simulations.

The form for the linear source representation of the spall model is such that it can easily be added to a one-dimensional (1-D) explosion source to compute regional and teleseismic synthetic seismograms. In a companion paper, McLaughlin, *et al.* (1990), use the model to compute the effects of spall on synthetic regional explosion seismograms. It is found that the spall contribution to the Lg signal is comparable to the direct explosion contribution. Their work is summarized in Section III of this report.

The Tension Crack Model

We have extended the circular tension crack model of Day, *et al.* (1983) to include a time dependence which describes the detachment and slap-down of the spall volume. The spall volume in the model is defined as the cylinder whose radius is that of the tension crack and which extends from the crack to the surface (Figure 2.1). Since we wish to compare the spall model with 2-D simulations which were done in a layered medium, we developed the formalism for computing the far-field body waves emanating from a layered medium. We briefly describe the features of the model and refer the reader to Barker and Day (1990) for derivations and details. The parameters of the model are the crack radius and depth, and the distribution of detachment velocities over the crack. In the complete model, as described in Barker and Day, the tension crack opening is tied to the arrival time along the spall surface of the reflected tensile wave pP. In addition, the initial opening velocity varies smoothly over the spall surface. The spall volume then decelerates under gravity until it closes.

The general behavior of the model can be illustrated for the analytically simpler case in which the crack opens simultaneously over the whole spall surface, and the initial velocity is uniformly distributed over the surface and over the velocity range v_1 to v_2. In that case, we can approximate the far-field P-wave displacement along the ray by

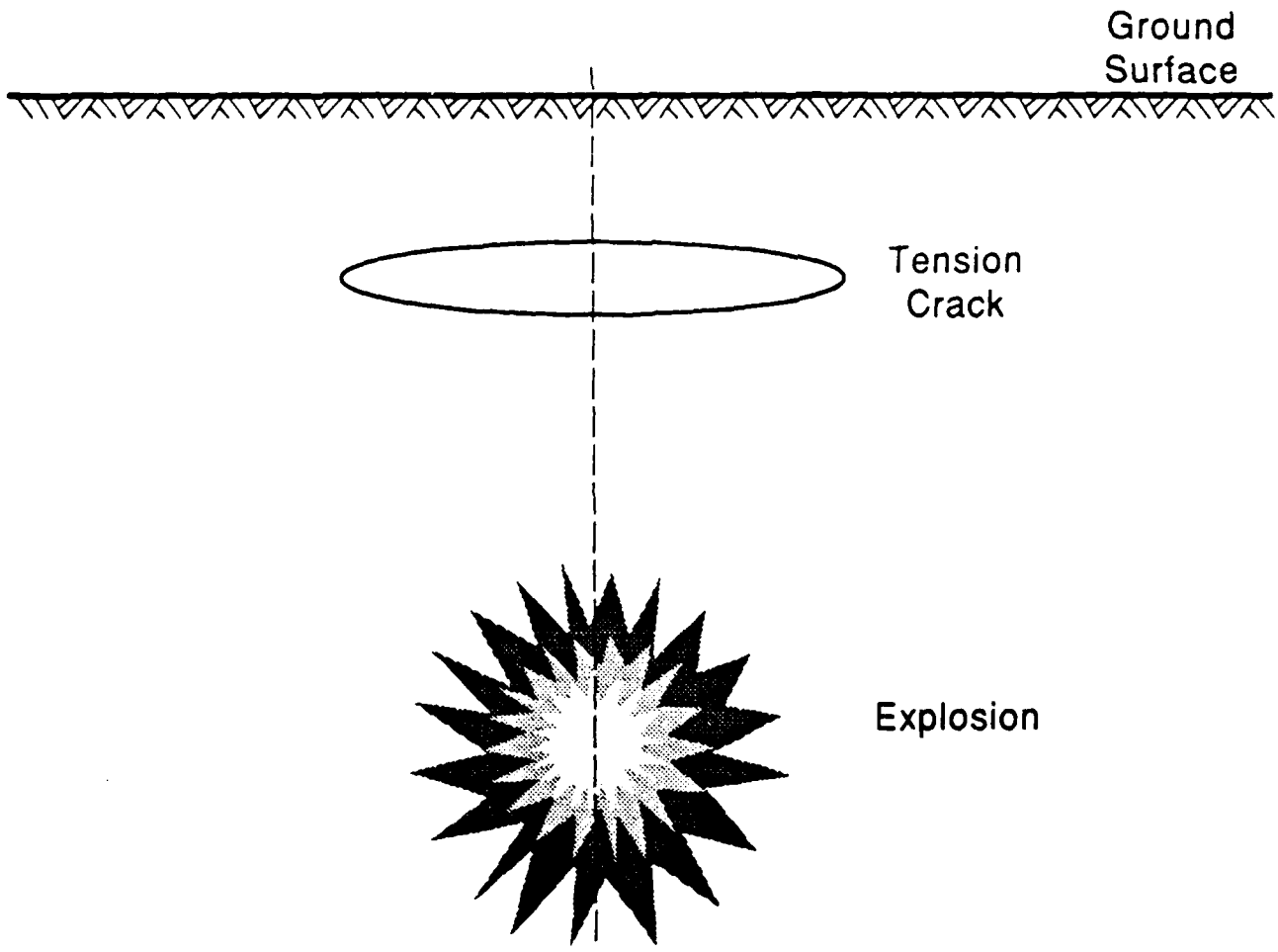

Figure 2.1. The tension crack model for spall.

$$u^P_{ray}(t) = \frac{z_s}{p^2\alpha^2 R}\,[(ap)^2-t^2]^{1/2} * \ddot{S}_0(t) \quad , \quad -ap \le t \le ap \quad , \tag{1}$$

where p is the ray parameter, a is the radius of the tension crack, z_s is the depth of the crack, α is the P-wave speed at the source, R^{-1} is the geometric spreading factor, and * denotes convolution. The function $\ddot{S}_0(t)$ is the time history of the mean acceleration of the spall volume, and is given by

$$\ddot{S}_0(t) = \bar{v}\,\delta(t) - g\Delta H(0,t_1) + \left[\frac{g}{v_2-v_1}\right](-v_2+\frac{3}{4}gt)\,\Delta H(t_1,t_2) \quad . \tag{2}$$

Here, v_1 and v_2 are the the minimum and maximum detachment velocities on the crack, the times, $t_i=\frac{2v_i}{g}$, are the corresponding flight times, $\bar{v}$ is the mean detachment velocity, and

$$\Delta H(t_1,t_2) = H(t-t_1)-H(t-t_2)$$

is a "boxcar" turning on at t_1 and off at t_2. Equation (2) is shown schematically in Figure 2.2. The displacement time function $u^P_{ray}(t)$ is formed by convolving $\ddot{S}_0(t)$ with $(a^2p^2 - x^2)^{1/2}$, which results from the radial finiteness of the spall.

We note that typical teleseismic values of p are less than 0.1 sec/km, and values of a are around 1 km, so $ap < 0.1$ sec, which allows (1) to be further approximated by

$$u^P_{ray}(t) = \frac{m_{spall}}{2(\lambda+2\mu)R}\,[\,\bar{v}\,\delta(t) - g\Delta H(0,t_1) + \tag{4}$$

$$\frac{g}{v_2-v_1}\,(-v_2+\frac{3}{4}gt)\,\Delta H(t_1,t_2)\,]$$

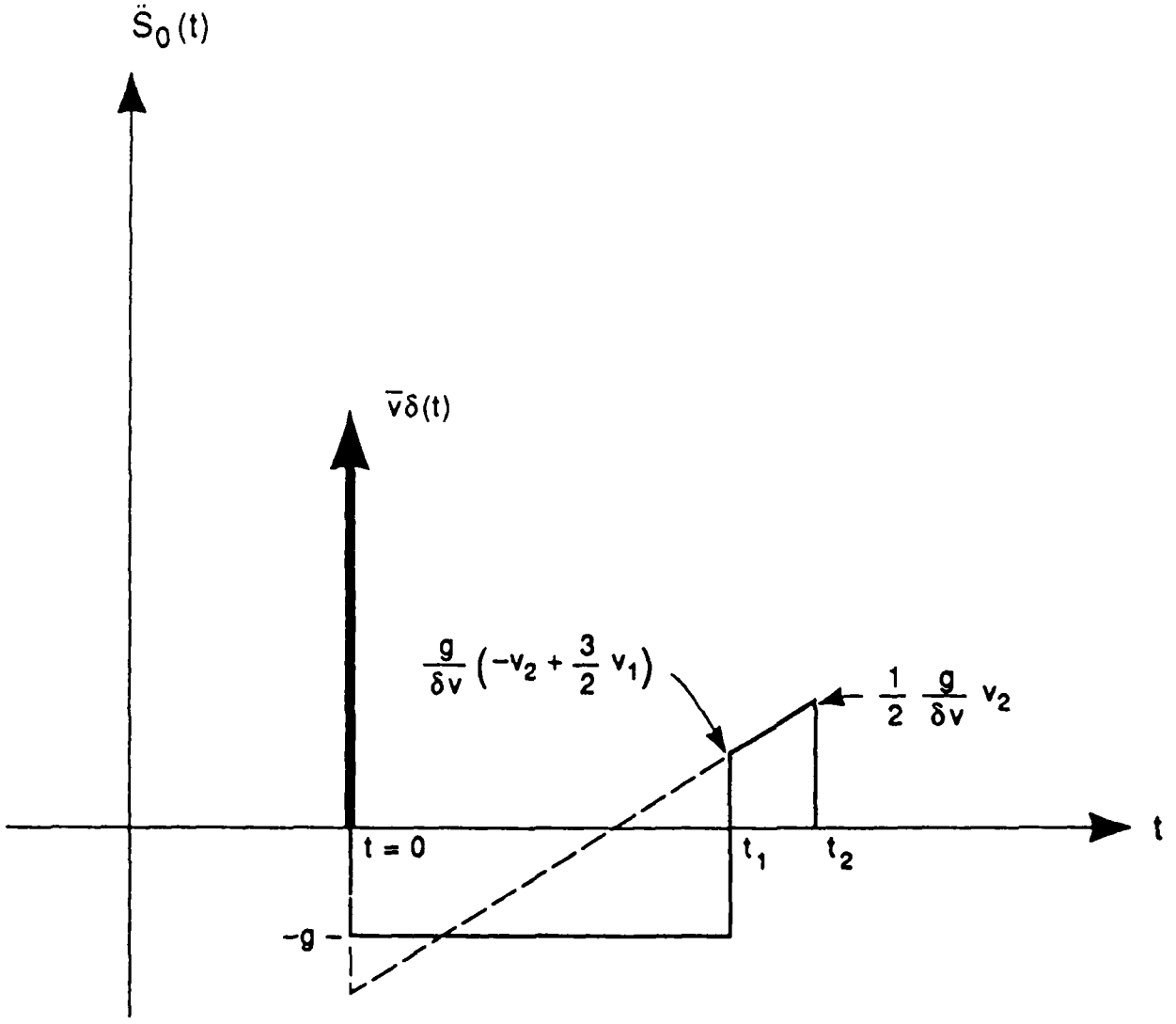

Figure 2.2. Schematic drawing of the detachment acceleration, which is proportional to the P-wave displacement for constant detachment velocity.

where m_{spall} is the mass of the spall volume, and λ and μ are the Lame' parameters at the source. The inital δ function term in (4) is proportional to $m_{spall}\bar{v}$, the mean spall momentum. The dwell term is proportional to $m_{spall}g$, the gravitational restoring force. The duration of the dwell is t_1, and that of the slap down is t_2-t_1.

The spectrum of the tension crack is shown schematically in Figure 2.3. It is peaked near the frequency $f_{pk} = (t_2-t_1)^{-1}$. Typical maximum detachment velocities are between 1 and 10 m/sec, so values of t_2 are .2 to 2 sec. Assuming the minimum velocity v_1 is nearly zero, f_{pk} would be in the range 0.5 to 5. Hz, which puts the peak right in the teleseismic and regional frequency bands. The rate of roll-off at high frequencies depends on the spatial dependence of detachment velocity, but for any distribution which goes to zero at the edge of the crack, the rate is at least as fast as $\omega^{-5/2}$. The spectrum in Figure 2.3 rolls off at both high and low frequencies faster than explosion source functions, so that the effects of spall on the seismic signal are limited to a narrow frequency band.

Comparison with Numerical Simulations

The objective of this study was to derive a simple, linear physical model which represents the spall process. Our strategy has been to isolate surface interaction effects by comparing the wavefields from 2-D calculations, u_{2-D}, with those from 1-D calculations done, u_{1-D}, in the same source materials (but in an inifinite medium). Our working assumption is that the difference in the

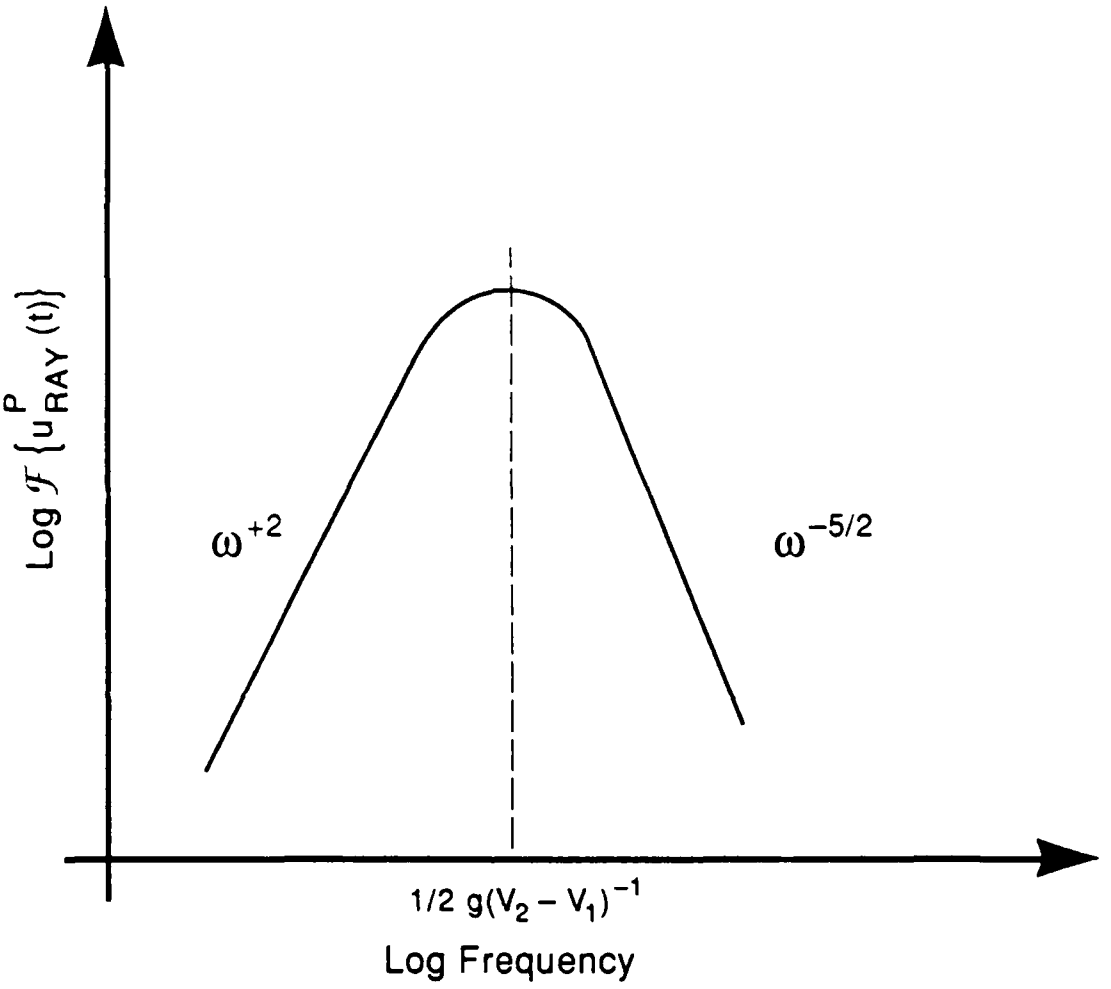

Figure 2.3. Spectrum of far-field P-waves from the tension crack model.

wavefields represents the free-surface interaction effects. In fact, the procedure has been to find the difference in the displacements $u_{2-D}-u_{1-D}$, and find the parameters of the spall model (described in the previous section) which have displacements u_{spall} which best satisfy $u_{spall} = u_{2-D}-u_{1-D}$. Alternatively, we could have found u_{spall} which satisfies $u_{1-D}+u_{spall} = u_{2-D}$. We found the first approach to be more direct.

To find the ground motions from the 2-D calculations, we used the methods described in Rodi, *et al.* (1978), Bache, *et al.* (1982), and Day, *et al.*, (1983, 1986). The 2-D simulations themselves are described in Day *et al.* (1986). The elastic properties for the Pahute Mesa and Shagan River simulations are shown in Table 2.1. The method for computing the body waves entails evaluating a form of the elastodynamic representation theorem, which gives the motions in terms of spatial and temporal convolutions of displacements and stresses monitored on a surface surrounding the nonlinear zone with Green's functions and their spatial gradients.

Table 2.1			
Elastic Structure for the Shagan River Simulations			
Layer Thickness (m)	Compressional Velocity (m/sec)	Shear Velocity (m/sec)	Density Kg/ m^3
∞	5018	2789	2700
Elastic Structure for the Pahute Mesa Simulations			
Layer Thickness (m)	Compressional Velocity (m/sec)	Shear Velocity (m/sec)	Density Kg/ m^3
112.5	1208	661.4	1600
457.5	2025	1109	1950
∞	2887	1581	2000

Shagan River Simulations

We begin with the Shagan River simulations, which were all done at a yield of 125 KT and at four depths of burial (DOB): an over buried depth (980 m), an optimally buried depth (680 m), a depth just below cratering (no ejecta) (300 m), and a depth which causes cratering (200 m). The scaled depths of burial are 196, 120, 60 and 40 $m\ KT^{-1/3}$. The results for P-waves were presented in Day, *et al.* (1986), and we include them here for purposes of comparing with the spall model. As can be seen in Table 2.1, the earth model is a half-space, which reflects our lack of detailed knowledge of the structure rather than making a statement of homogeneity at the site. The far-field P and SV displacements are shown for a take-off angle of 10° in Figures 2.4 and 2.5. In our detailed report (Barker and Day, 1990), we make comparisons at three take-off angles, 10°, 20° and 30°, which are representative of teleseismic, intermediate and

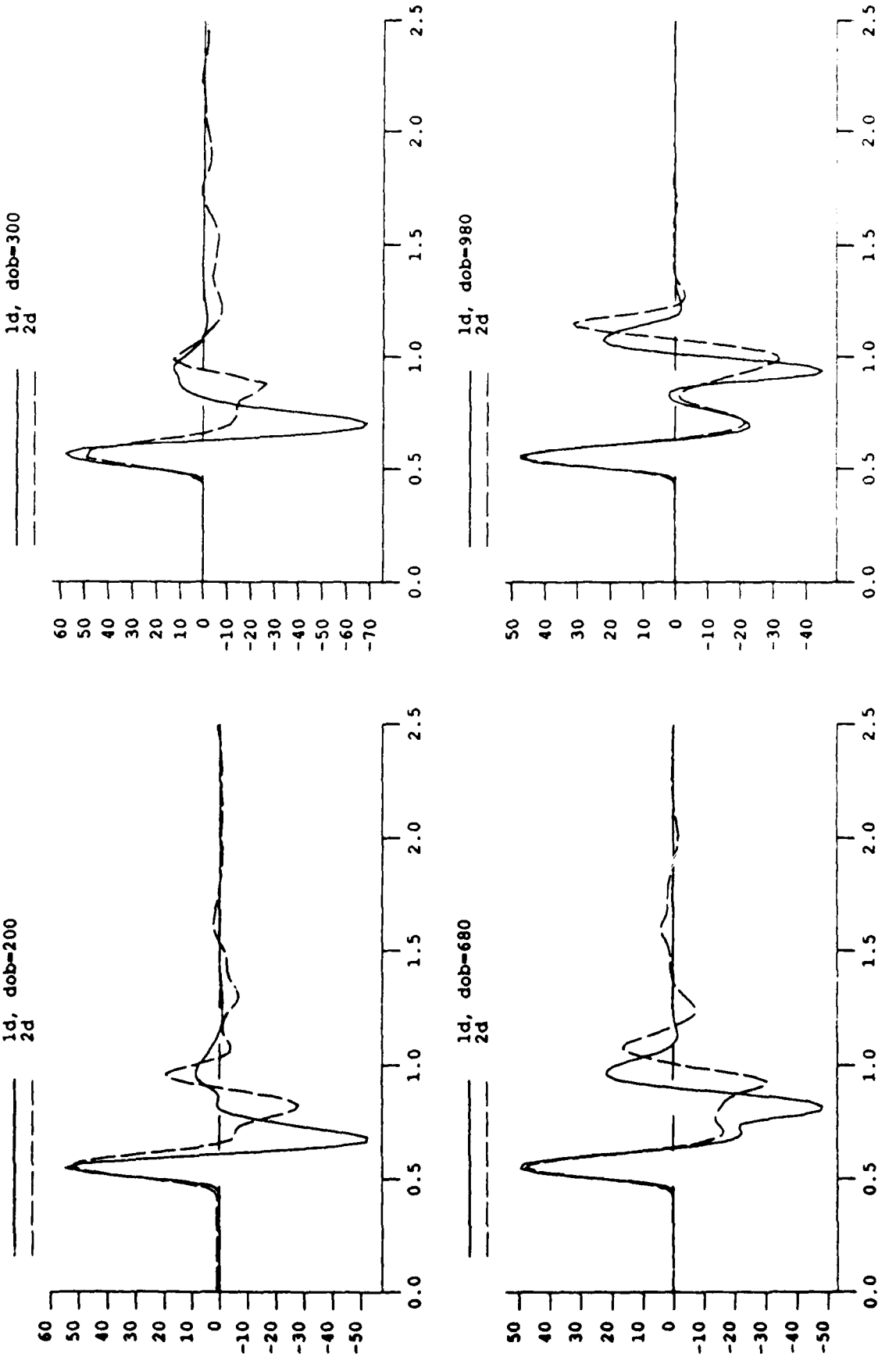

Figure 2.4. Comparison of the far-field P-waves from the 1-D (solid lines) and 2-D (dashed lines) Shagan River simulations for four depths of burial at a take-off angle of 10°.

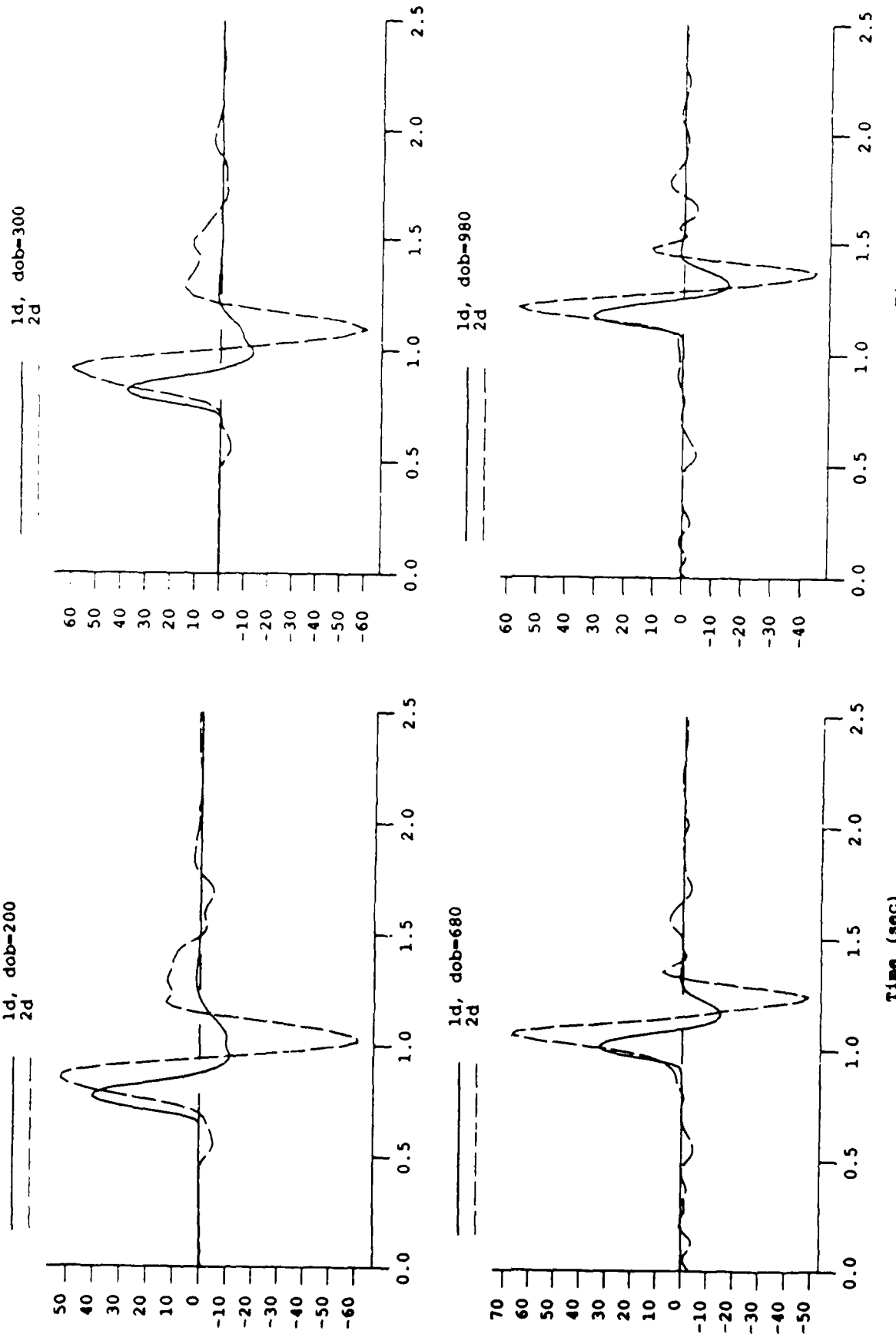

Figure 2.5. Comparison of the far-field SV-waves from the 1-D (solid lines) and 2-D (dashed lines) Shagan River simulations for four depths of burial at a take-off angle of 10°.

regional slownesses (phase velocities) for this source structure. These comparisons ensure that the spatial dependence is modeled correctly. In Figures 2.4 and 2.5, the motions from the 2-D simulations are overlain with 1-D simulations in which the nonlinear properties at the source are the same as the 2-D values. The 1-D source (RDP) was extracted, and the body waves were calculated for a linear elastic medium. Thus, for the Shagan River half-space model, the 1-D waveforms have the direct P phase, as well as the pP and pS elastic reflections. These signals correspond to down-going, teleseismic ray paths, but do not include the effects of mantle or crustal propagation, anelastic attenuation, or recording instrumentation.

The rise time and amplitude of the first peak in the P-waves (Figure 2.4) is very nearly the same for the 1-D and 2-D calculations. For the shallow calculations (200 and 300 m) the 1-D and 2-D waveforms diverge after the peak and are quite different at later times, indicating that the cratering and near-cratering processes are indeed different from elastic pP reflections. For the deeper DOB's, 680 and 980 meters, the apparent pP phase on the 2-D records appears to be smaller, to have longer period, and to be delayed relative to the elastic pP (1-D) case.

The SV-waves (Figure 2.5) show much greater differences between the 1-D and 2-D cases. The 2-D solutions have a direct S-wave, due to vertical asymmetries in the source, which is not in the 1-D solutions. The main peaks in the 2-D SV-waves are larger than the 1-D peaks at all four DOB's, and are about twice as big for the 300, 680 and 980 depths. The duration of the main

peaks is also greater for the 2-D cases. A large negative swing occurs on the 2-D waveforms, which is much smaller on the 1-D signals.

As discussed above, we computed the 2D-1D difference waveforms and matched them to those from the spall model. The parameters of the spall model which most closely matched the numerical simulations are:

Table 2.2
Spall Model Parameters for the Shagan River Simulations

Depth of Burial z_{exp} (m)	Crack Depth z_s (m)	Crack Radius a (m)	Minimum Detachment Velocity v_1 (m/sec)	Maximum Detachment Velocity v_2 (m/sec)
200	100	600	1.1	20.0
300	150	600	1.1	15.0
680	200	600	1.1	4.0
980	200	600	1.1	1.5

In Figure 2.6, we compare the P-wave spall model waveforms with the 2D-1D waveforms for each of the DOB's. In general, the comparisons are quite good, both in amplitude and shape. The parameter that varies the most in Table 2.2 is the maximum detachment velocity v_2. Recall that in Equation (4), v_2 enters the solution in two ways. First, the δ function term, which causes the first peak in the waveforms, is proportional to the mean detachment velocity $\bar{v}$. Second, the duration of the signal (end of slap-down) is time $t_2 = 2v_2/g$. As the DOB decreases, the 2D-1D difference waveforms increase in amplitude and duration. Thus, as the DOB decreases, v_2 is required to increase. We note that, even in the case where cratering occured (200 m), the tension crack model provided a good representation of the P radiation. The shapes of the signals for the 980

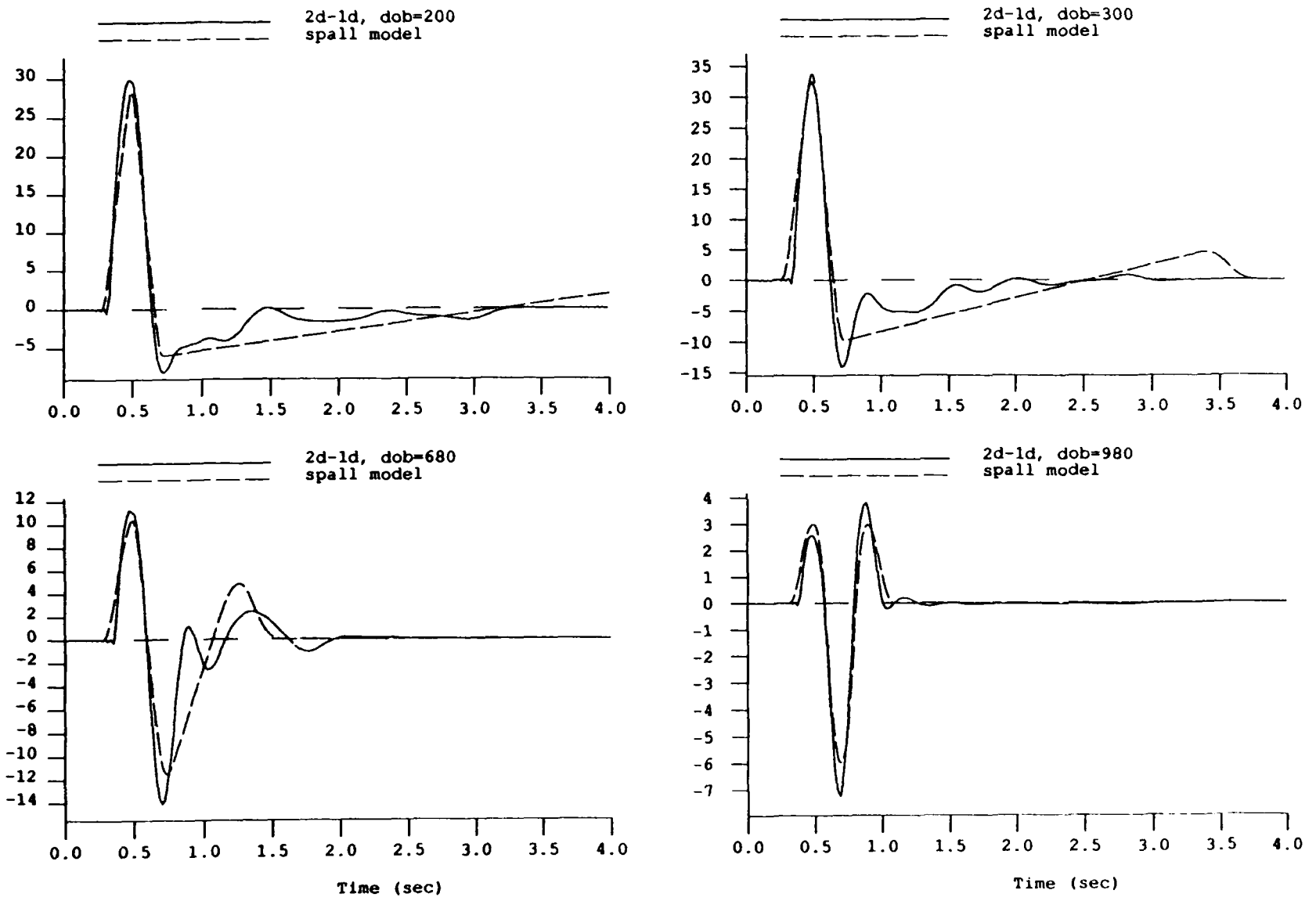

Figure 2.6. Comparison of the differential 2D-1D P-wave solutions from the Shagan River simulation with the tension crack P-waves.

meters case agree well. For the 680 meters case, the agreement is good except for an additional inflection in the later parts of the 2-D waveforms that is not modeled by the tension crack.

The peak detachment velocity is inferred from field observations from ground motion records at or near ground zero. We can do an analogous measurement by examining the vertical velocity in the finite difference simulation at the free-surface of the grid. We find that the values of v_2 in Table 2.2 agree closely with the ground zero velocities in the simulations.

Using the parameters in Table 2.2, we computed the SV-waves from the tension crack model and compared them with the corresponding 2D-1D difference SV-waves. As can be seen in Figure 2.7, the comparisons are not as good as the P-waves, especially at the deeper DOB's, where the amplitudes predicted by the model are too small by factors of two to three. Attempts to find a set of parameters which would improve the SV comparisons without degrading the P comparisons were unsuccesful. We note that in all cases, the tension crack models derived from the P-waves account for only a fraction of the SV radiation from the nonlinear simulations.

The results of the SV comparisons suggest that additional sources of SV radiation be incorporated. We therefore tried some additions to the model to improve this situation. First, we hypothesized that processes transpired in the simulations that could be represented as modifications to the isotropic part of the moment tensor. We chose to represent this as a compensated linear vector dipole, CLVD (e.g., Knopoff and Randall, 1970). The CLVD represents a

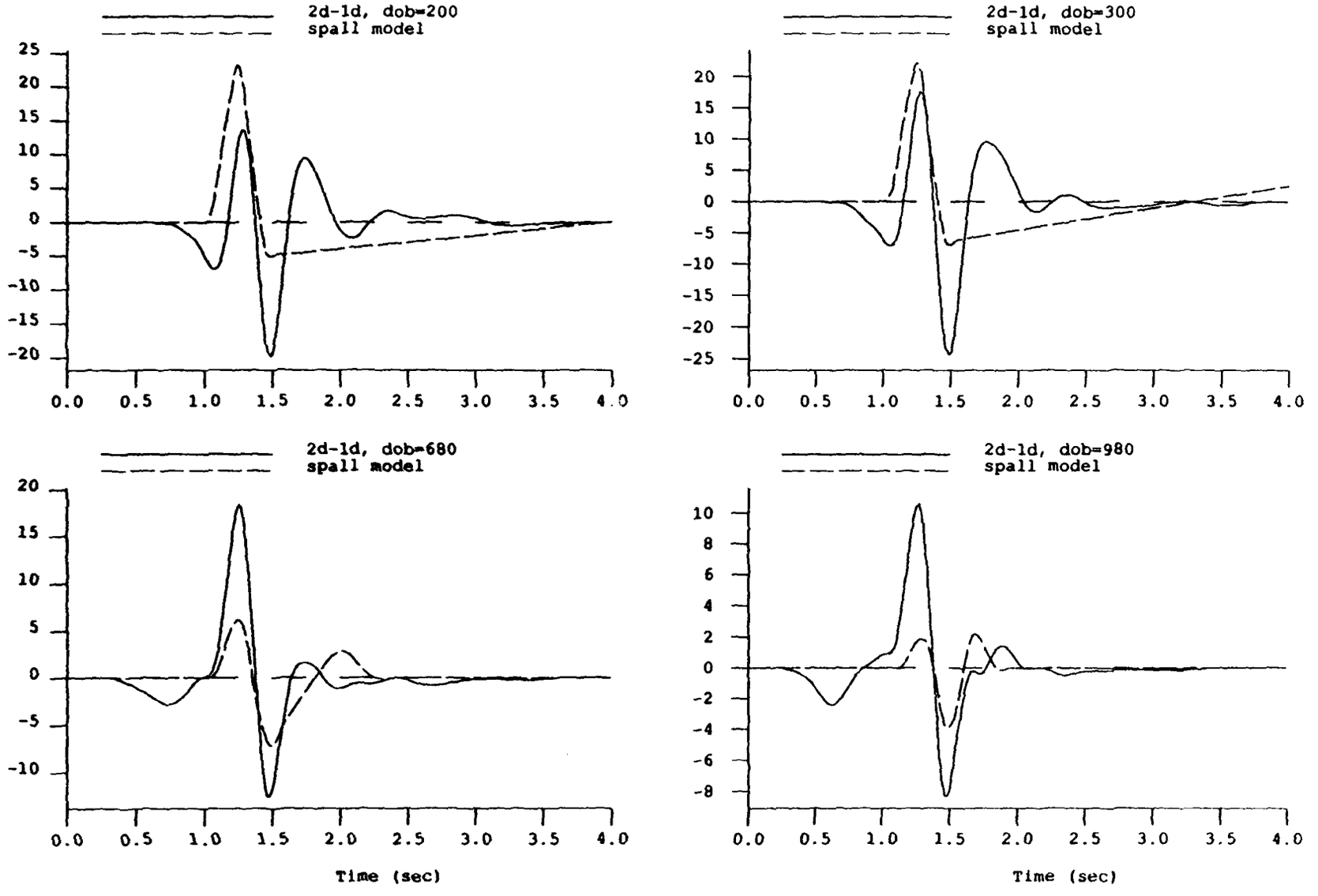

Figure 2.7. Comparison of the differential 2D-1D S-wave solutions from the Shagan River simulation with the tension crack SV-waves.

process akin to squeezing a vertical tube of toothpaste. We also hypothesized that additional sources of shear waves may be emanating from vertical cracks which are the boundaries of a cylinder which moves above the horizontal tension crack. That is, we imagine that the material above the tension crack moves up and down as a unit, shaped as a cylinder whose base is the tension crack. The relative motion along the vertical sides would act as a distributed shear dislocation. In Barker and Day (1990), we compare the SV-waves from these two models with the 2D-1D waveforms. The CLVD source when added to the tension crack source in various proportions produced SV-waves that were large enough to fit the 2D-1D difference waveforms, and the shape of the waveforms agreed well. Since the CLVD source generated small amounts of P-waves, the goodness of fit to the P-waves seen above was not affected. However, the proportions were different for each DOB, which effectively added another free parameter whose interpretation was ambiguous. The distributed shear dislocation source (the moving cylinder described above) produced SV-waves that were too small, and so it appears that the cylindrical source is not a likely candidate for additional SV radiation.

Pahute Mesa Simulations

The 2-D and 1-D P-wave signals for the Pahute Mesa simulations are overlain in Figure 2.8 for a take-off angle 3.3^o. The calculations were done at DOB's of 200, 680 and 980 m for the Pahute Mesa model, but not at 300 m. The first peaks of the 1-D and 2-D signals align closely. For DOB's 680 and

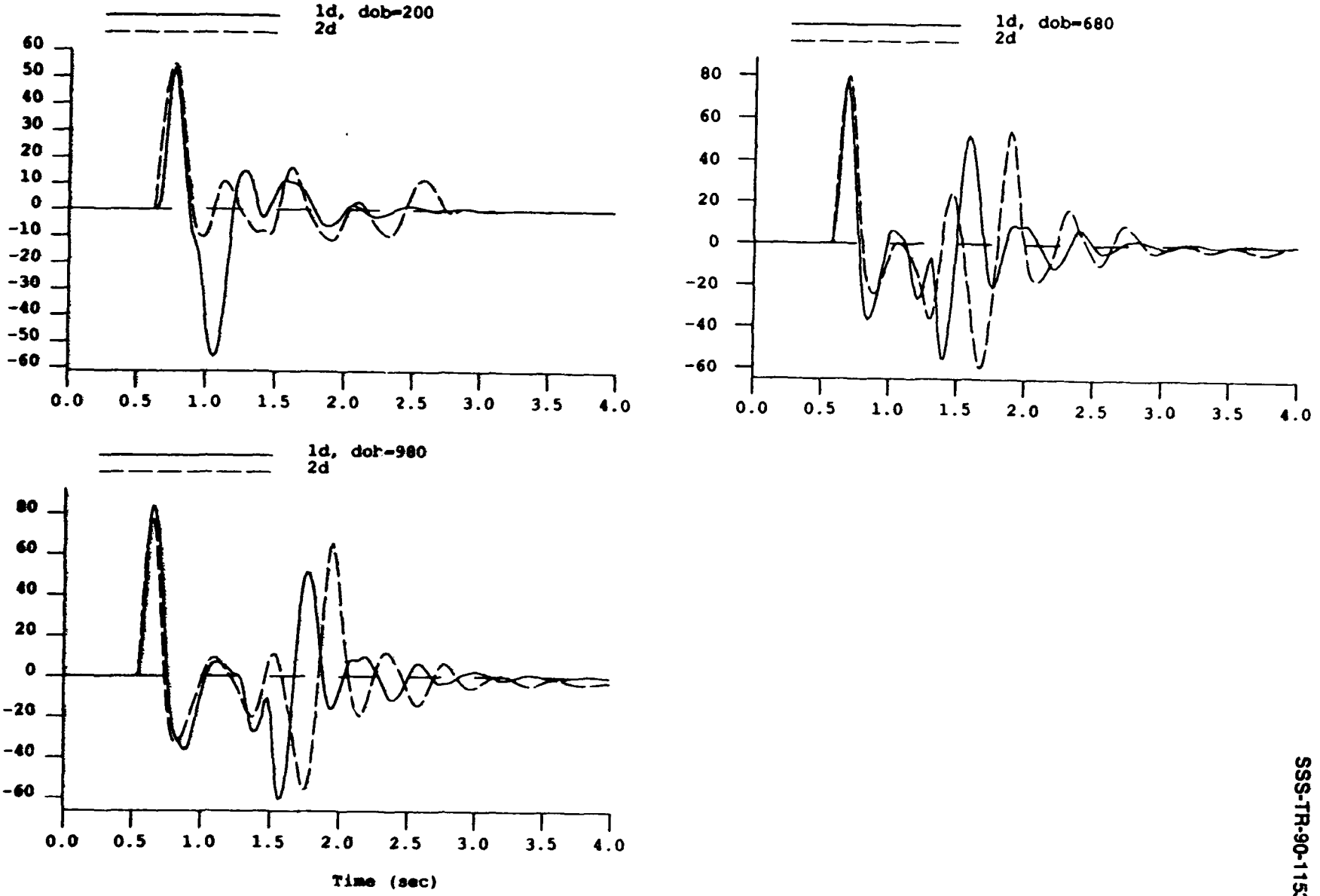

Figure 2.8. Comparison of the far-field P-waves solutions from the 1-D (solid lines) and 2-D (dashed lines) Pahute Mesa simulations for three depths of burial at a take-off angle of 3.3°.

980, the apparent pP from the 2-D waveforms is lagged about 0.2 seconds relative to the elastic pP in the 1-D waveforms.

As with the Shagan River simulations, we fit the tension crack model to the 2D-1D difference time series. The results are shown in the comparison plot in Figure 2.9. The fits of the model to the differential 2D-1D signals are generally good for the three DOB's and take-off angles. The best fitting parameters of the model are

Table 2.3
Spall Model Parameters for the Pahute Mesa Simulations

Depth of Burial z_{exp} (m)	Crack Depth z_s (m)	Crack Radius a (m)	Minimum Detachment Velocity v_1 (m/sec)	Maximum Detachment Velocity v_2 (m/sec)
200	150	400	1.1	22
680	200	2200	1.1	2
980	150	2200	1.1	2

There are several differences between the model parameters derived here and those for the Shagan River simulations. First, we found for the Pahute Mesa runs that the detachment velocity must be distributed over the crack with the largest values near the center in order to match the change in 2D-1D signals with take-off angle. This is in contrast to the Shagan River case, where the solutions were insensitive to the form of the distribution. This difference is due to the velocity structures, where the Shagan River wave speeds, and hence the phase velocities, are about twice those of Pahute Mesa.

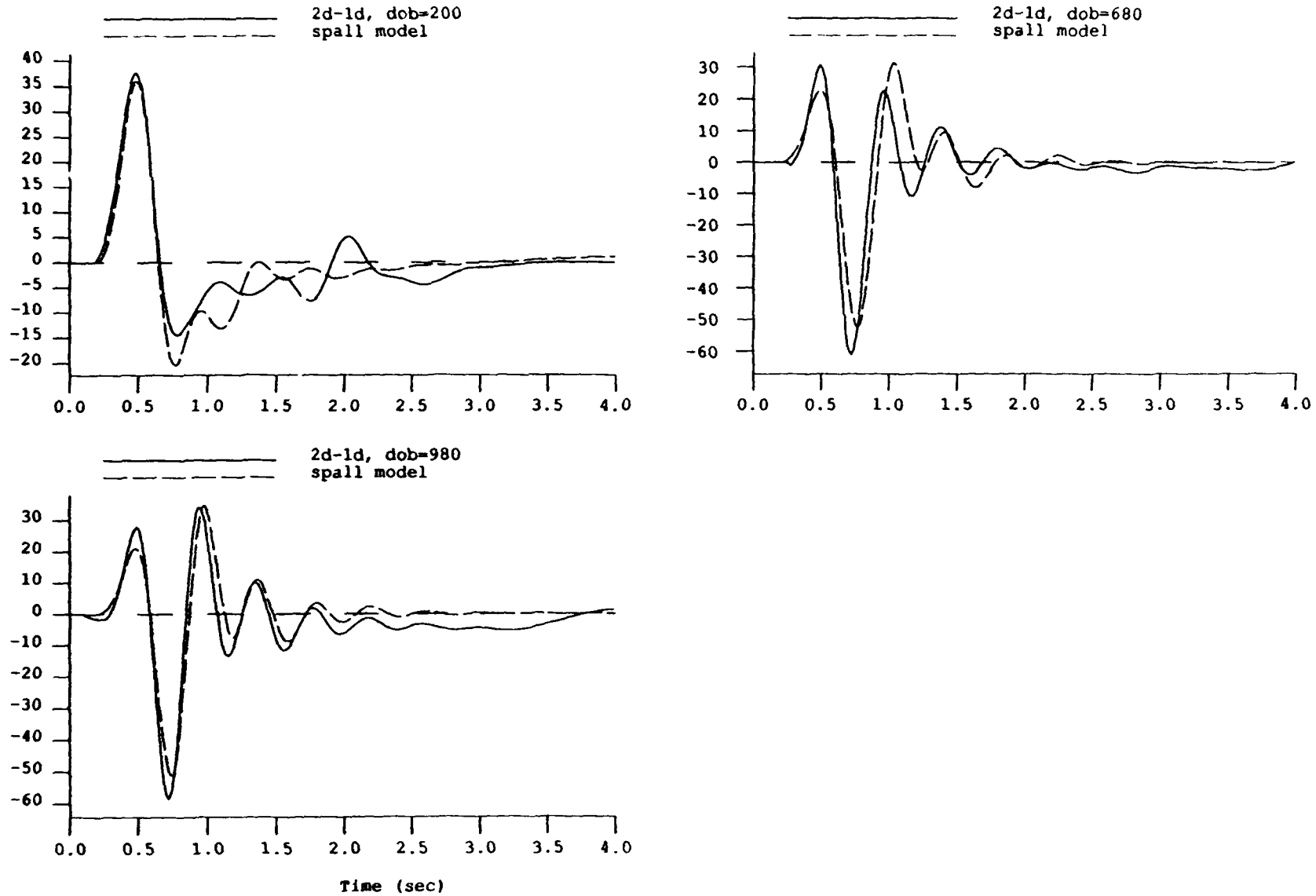

Figure 2.9. Comparison of the differential 2D-1D P-wave solutions from the Pahute Mesa simulations with the tension crack P-waves.

Another feature of the Pahute Mesa simulations that differs from the Shagan River runs is the large change in crack radius between the case for DOB=200 and the other two DOB's. This is presumably due to the shallow layering in the Pahute Mesa earth model. Although the tension crack had a maximum detachment velocity (22 m/sec) similar to Shagan, it occurred over a much smaller radius (400 m).

The results of the comparisons of the SV-waves from the tension crack model in Table 2.3 are similar to those for the Shagan River simulations discussed above. The tension crack generates SV-waves that are too small.

Comparisons with Observations

From observations of surface ground motions and of physical manifestations of Pahute Mesa tests, several authors have estimated the parameters of the spall process. In Table 2.4, we compare their results with those for the tension crack model at the optimal DOB (680m).

Table 2.4. Spall parameters from field observations and from the tension crack model for Pahute Mesa

Parameter	Tension Crack	Patton (1990)	Sobel (1978)	Viecelli (1973)	Stump (1985)	Rawson (1988)
Maximum Velocity (m/sec)	2	6.4		8		
Radius (m)	2200	1750		500		500-2665
Momentum ($\times 10^{12}$ Nt-s)	7.5	9.2	3.5	0.58		
Mass ($\times 10^{12}$ Kg)	5.3	3.5	1.2	0.2	3.0	
Depth (m)	200			110		100-400

The authors cited in the table typically expressed their results as scaled values, in which case we used 125 KT, the yield in the simulations. In addition, the values in Table 2.4 are the average values given by the authors. The mean detachment velocity (1.55 m/sec) was used to compute the tension crack momentum, rather than the mean velocity. The momentum, spall radius and depth from the tension crack model lie within the spread of those inferred from observations. The mass is at the high end while the maximum velocity is at the low end.

It is very difficult to estimate the parameters in Table 2.4 because of a paucity of direct observations. There are typically few surface ground motion sensors, and no sub-surface observations of ground motion or other phenomena such as cracking. Inference of the spall process beyond estimating apparent pP amplitude and travel time from far-field recordings has not been successful.

With these limitations in mind, it can be said that the parameters of this study are consistent with published field observations.

Summary and Conclusions

We show that a simple model can be constructed which generates the far-field P-waves of a two-dimensional nonlinear calculation which includes the effects of the free-surface for a range of depths-of-burial. The model which fits the P-waves from the simulations underestimates the SV-waves. The model, proposed in its original form by Day, *et al.* (1983), is based on using a tension crack which opens due to the tension wave from the free-surface. The material over the crack travels up with the impulse of the tension wave and returns under the influence of gravity. Stump (1985) modified the original model to include the effects of source by adding an empirical time function based on chemical explosions. The modified model was used by Taylor and Randall (1988) to model regional seismograms. In our formalism presented in this report, we include the effects of source finiteness and those of crustal reverberations. A time dependence is a natural consequence.

The parameters of the model compare favorably with observations based on field data. In addition, McLaughlin, *et al.* (1990), use the model to compute regional seismograms and find that in the Lg bandwidth, the spall contribution should be comparable to or greater than that of the explosion signal alone. Since the spall model which fits the P-waves in our study generates SV-waves

that are too small, the spall model may lead to an underestimate of the Lg from spall. Spall, therefore, appears to be a very significant source of Lg.

Section III

Implications of Explosion Generated Spall Models: Regional Seismic Signals

Spall is a frequently observed phenomenon associated with the free surface reflection of an explosion generated compressional wave. The compressional wave originating from an underground explosion becomes a tensional wave upon reflection from the free-surface. If the rock near the free-surface fails under this tension then the volume of material above the tensile failure goes into ballistic free-fall. This free-fall is often recognized by acceleration records above the explosion that exhibit -1 g dwells (free fall) followed by a sudden slap down. During this free fall the motion of the material is largely governed by the force of gravity. A number of authors have gathered data concerning spall from both underground nuclear explosions and contained chemical blasts (Eisler and Chilton, 1964; Viecelli, 1973; Sobel 1978; Stump, 1985; Patton, 1990). The Day, *et al.* (1983) seismic representation for spall has become a widely accepted model for the source representation of this nonlinear phenomenon. This model has been modified and used by Stump (1985), Patton (1988), and Taylor and Randall (1989) to model near-field and regional seismic phases due to spall. The models for spall considered here are based on the original Day, *et al.* (1983) tension crack representation for spall and modified to include a distribution of spall over the zone of tensile failure as parameterized by Barker and Day (1990).

Assessing the importance of spall in exciting regional seismic signals requires a physically reasonable and consistent model for the forces and/or moment tensor expansion of those forces. These representations may then be used to make predictions of the spall signal and to invert for possible spall models using far-field seismic data.

Section II of this report summarizes the results from modeling 2-D axisymmetric nonlinear finite difference calculations. In these simulations, spall was observed and the equivalent seismic sources from the calculations were modeled as a point explosion plus the opening and closing of a tension crack (spall). Such a model is illustrated in Figure 3.1. In this section, we summarize results of calculations that attempt to use these models to predict regional phases such as Pg, Lg, and Rg. The physically reasonable spall models are used to derive consistent models for the equivalent moment tensor representations for the seismic source. These moment tensor sources are then used in conjunction with wavenumber integration Green's functions for the response of a layered earth structure to compute synthetic regional seismograms.

As part of this work we present a new derivation for the approximate equivalence of the surface point force and the moment tensor representations of a buried tension crack. The approximation is tested numerically and found to be adequate for tension cracks buried less than 1/4 of the shear wave wavelength for Pg and Lg. Proper modeling of Rg requires wavelengths longer than eight times the burial depth. In addition, a smoothing operator, E(t), is presented that results from a model of finite extent of the spall distributed over

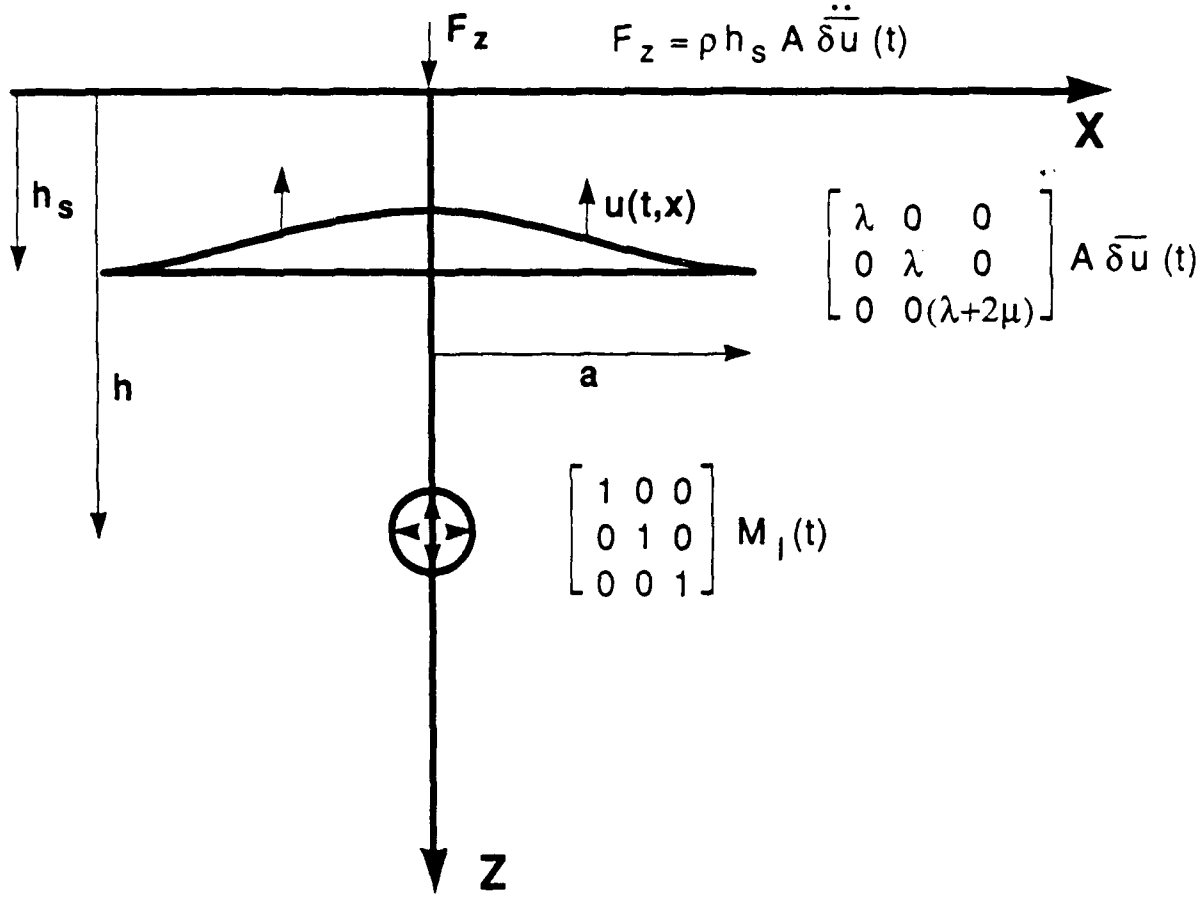

Figure 3.1. The axisymmetric spall above the explosion is modeled as a circular horizontal tension crack that opens and closes in the vertical direction. The spall is parameterized by the source depth h_s, the crack radius a, and the displacement time function u(t,x). The radiation from a horizontal tension crack is equivalent at low frequencies to the radiation from a vertical point force, F_z, at the surface proportional to the second time derivative of δu. The moment tensor source representation for the tension crack is proportional to δu. A is the area of the crack, ρ is the density, and λ and μ are the Lame parametes for the medium.

the tension crack. In this model, motion is zero at the crack tip and spall motion is concave upward. Such a model implies that the spall source falls-off at high frequencies at least as fast as $\omega^{-5/2}$. Since the spall source is proportional to ω^2 for low frequencies and falls-off faster than ω^{-2} at high frequencies, the spall contribution will always be a narrowband signal compared to the explosion source which is flat at low frequencies and falls-off as ω^{-2}.

Figures 3.2 and 3.3 show the equivalent force time histories and their spectra for teleseismic P-wave, Pn, Pg, and Lg slownesses. Note that as a consequence of the finite extent of spall across the tension crack, the equivalent seismic source depends on the apparent slowness of the seismic phase. Phases with slower apparent velocities show a lower corner frequency and appear more narrowband. The spall momentum, depth, extent, and velocities are given by the Barker and Day (1990) parameterization for spall observed in the finite difference simulations for a 125 KT, 680 meter deep explosion in a Shagan River model.

Figure 3.4 shows the vertical displacement Lg and Pg waveforms predicted for a distance of 300 km from the explosion and the spall sources in Figures 3.2 and 3.3. The seismic sources have been convolved with the Green's functions for an explosive source and those for a tension crack to predict the regional ground motion from the two source components. Note that the spall source has an Lg 10 times larger than the explosion point source Lg. In contrast the spall source modulates the Pg signal interfering with the pP from the explosion to complicate the Pg waveform. Spectra are shown in Figure 3.5 to show that the

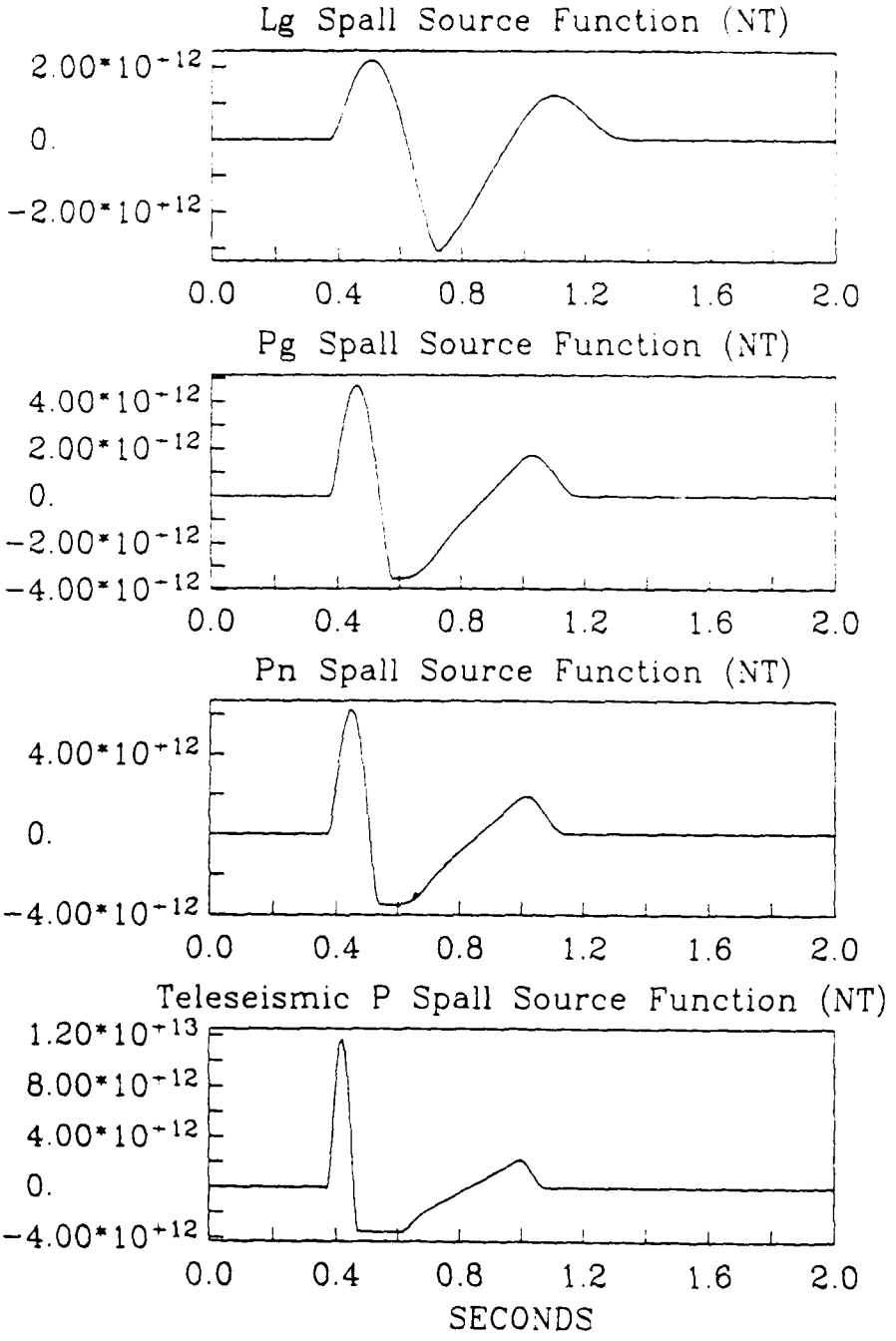

Figure 3.2. The equivalent spall source (for source depth of 680 m) for four different apparent phase velocities corresponding to teleseismic P, Pn, Pg, and Lg. The smoothing operator E(t) simulates the disk-like nature of the source as seen in the far field by a wave of a given slowness. Slower phases are more sensitive to the size of the spall disk. Because the spall velocity is distributed across the tension crack, the crack opens faster than it closes and the seismic source is asymmetrical. The slap down is distributed over a longer time period than the initial spall opening and therefore although the area under the curve is zero, the closing phase has lower frequency character than the opening phase.

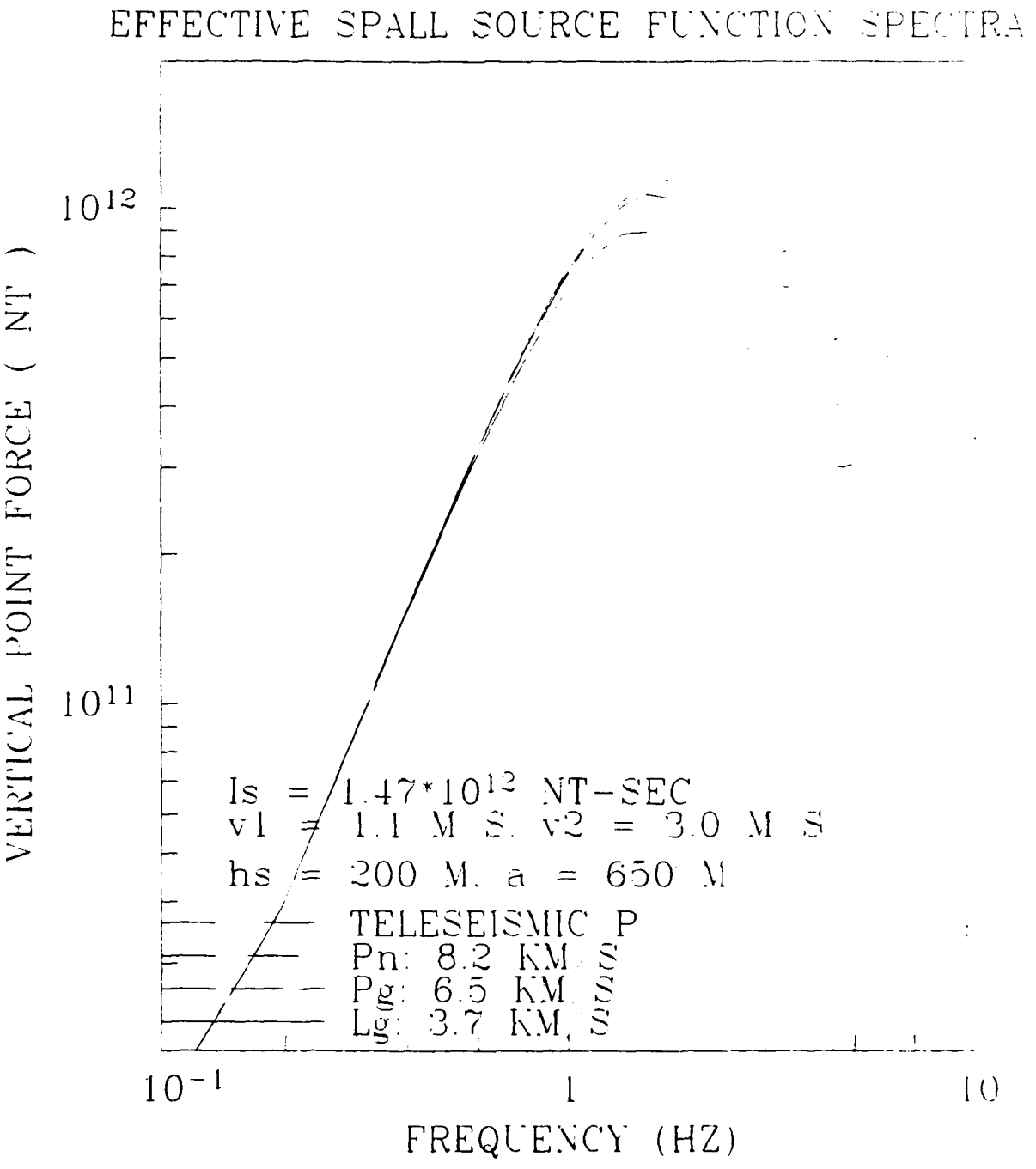

Figure 3.3. Spectra of the time series of Figure 3.2. The finite extent of the tension crack ensures that the slower phases like Lg have an equivalent spall source that falls-off more rapidly than the higher phase velocity phases such as Pg, Pn or the teleseismic P-wave equivalent spall source.

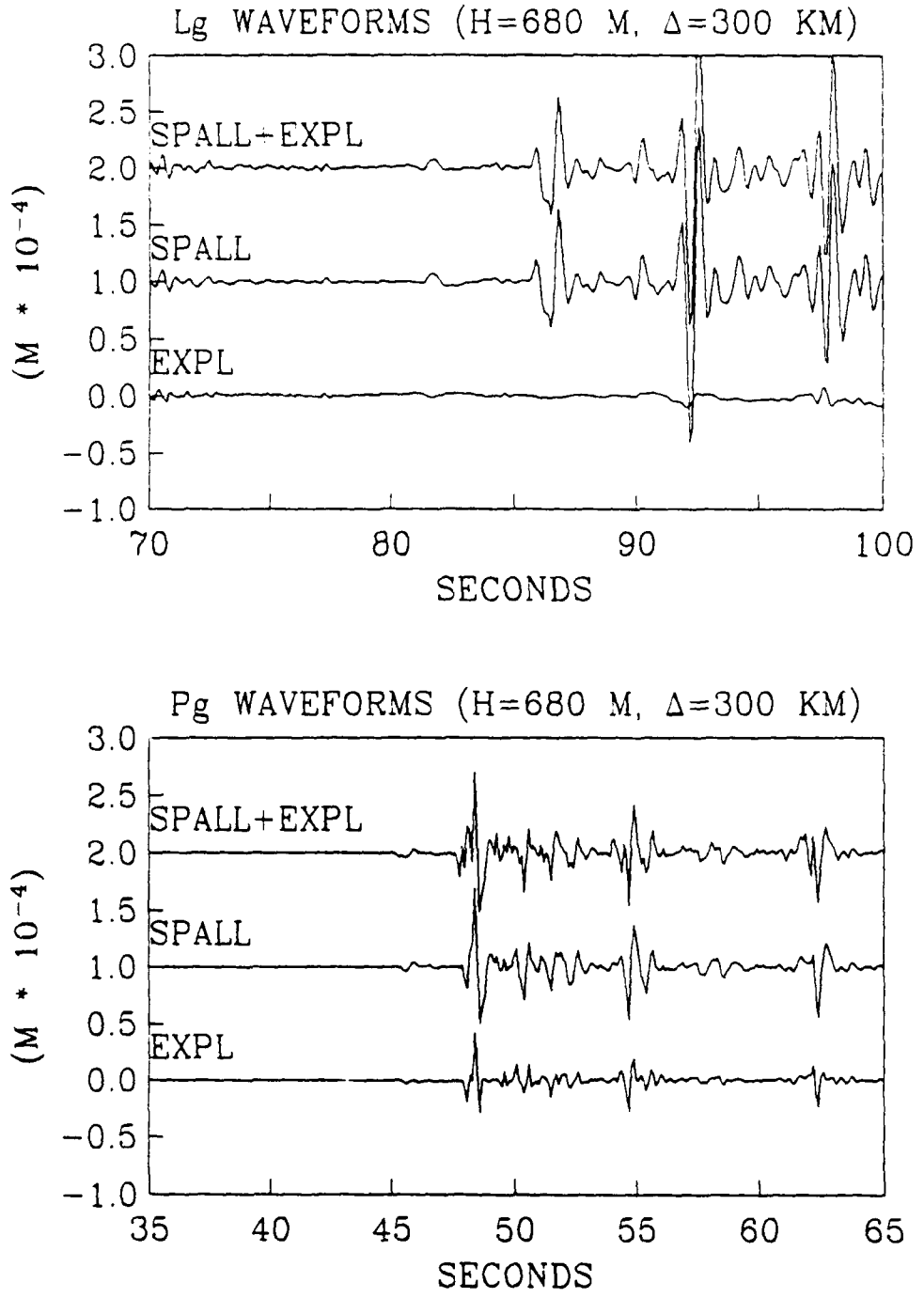

Figure 3.4. Synthetic Lg and Pg waveforms at a distance of 300 km for the 680 meter depth of burial 125 KT Shagan River explosion simulation. The spall model is from Barker and Day (1990) based on parameterized models derived from a nonlinear axisymmetric finite difference calculation. Note that the Lg spall signal dominates the Lg explosion signal while the Pg explosion+spall signal is only somewhat larger than the pure explosion Pg signal. The m_b(Lg) from the spall source is about 6.2. The m_b(Lg) from the pure explosion source is about 4.9.

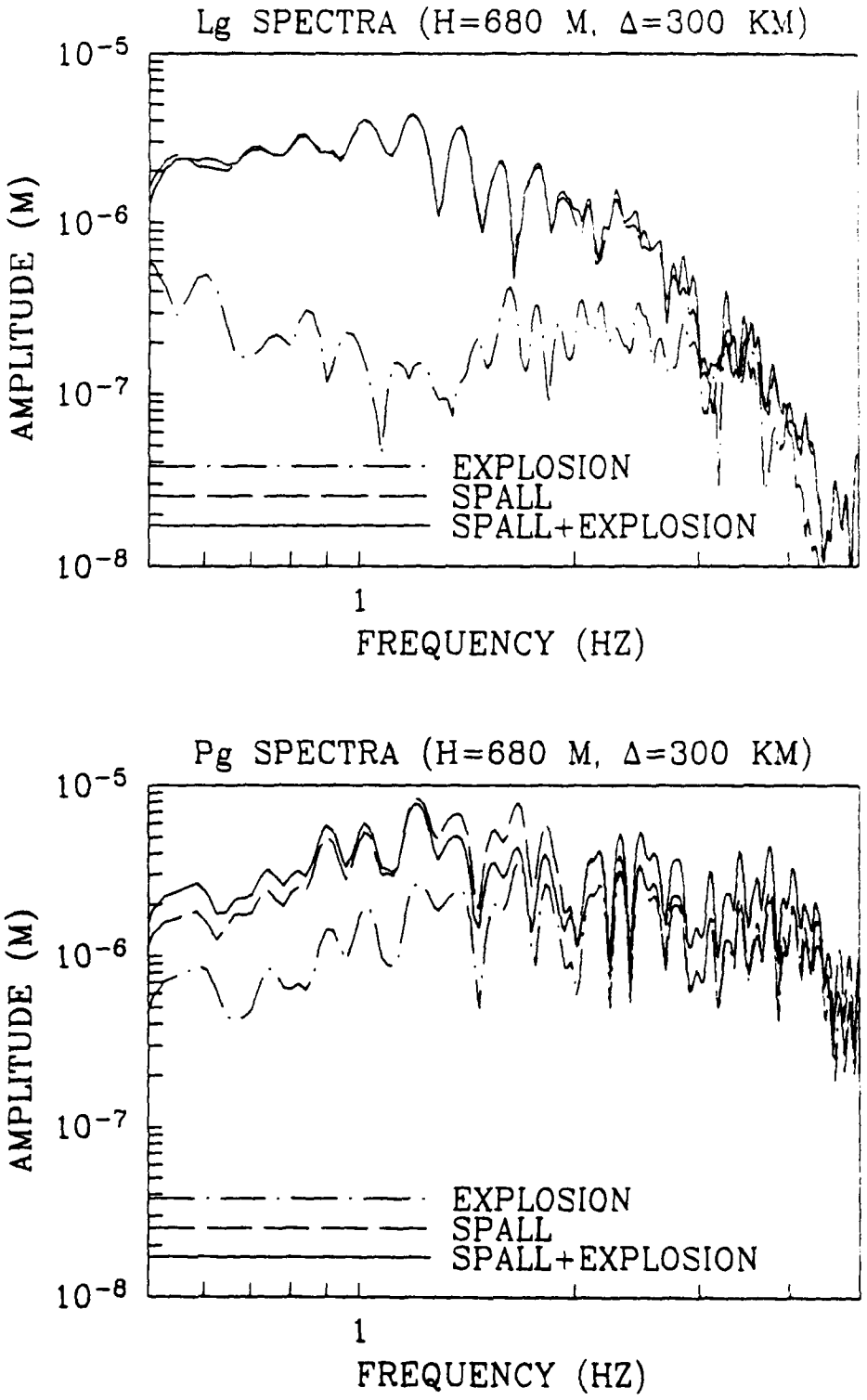

Figure 3.5. Spectra of the time series in Figure 3.4. The Lg spall signal is about 20 times larger than the Lg explosion signal at 1 Hz while the Pg spall signal is about two times larger than the pure explosion Pg signal at 1 Hz. The Lg spall signal is narrowband and falls-off rapidly below the Lg explosion signal above 3 Hz.

Lg is dominated by the spall source for frequencies up to 3 Hz. The spall source provides low frequencies below 1 Hz and the spall+explosion signal is closer to the average of the two sources at frequencies above 1 Hz.

We conclude that the parameterized spall models of Barker and Day (1990) predict significant Lg excitation relative to the point explosion part for Eastern Kazakhstan crustal models. As seen in Section IV, this is in contrast to crustal structures with low near surface velocities and high near surface attenuation as typical of basin and range NTS models. Crustal models with high near surface P-wave velocities exhibit very weak Lg excitation from point explosions. The shallow tension crack source in these models is a significant Lg source without overly dominating the Pg waveform. The parameterized models of Barker and Day (1990) based on the nonlinear finite difference simulations predict an m_b (Lg) ≈ 6.2 for the 125 KT explosion. In contrast the point explosion model in such a crustal structure predicts an m_b (Lg) ≈ 4.9.

While there are other hypotheses for the excitation of Lg from explosions, it is clear that for Eastern Kazakhstan structures, the spall model could be a significant contributor to the Lg signal. The point explosion is clearly a poor model for the Lg excited by an explosion in these structures. Even a small amount of spall will overcome the Lg excited by the pure explosion part of the source.

Section IV

Analysis of Pg and Lg Excitation by Axisymmetric Sources in Layered Anelastic Crustal Models

Background

Section III of this report summarizes work from McLaughlin, *et al.* (1990) that applies the Barker and Day (1990) parametric seismic source models summarized in Section II and shows they imply spall should be a significant source of Lg in addition to the pure explosive source. In order to put this conclusion into perspective, we report in this section on numerical calculations that demonstrate differences between Pg and Lg excitation by point explosion, spall, and CLVD sources in layered earth structures representative of the basin and range and the Eastern Kazakhstan regions. The crustal structures for these two regions are very different and lead to significant differences in theoretical Pg and Lg excitation by simple point sources. Generalizations about relative excitation of regional phases by different source types in one structure often do not apply in the other structure.

In addition to the simple point explosion source we examine the Pg and Lg excitation from axisymmetric deviatoric sources suggested by the spall models of Barker and Day. There have been previous studies that compare the excitation of Pg and Lg by shallow point explosions for purposes of examining the theoretical basis of explosion and earthquake discrimination, see for example, Campillo, *et al.* (1984), Bennett, *et al.* (1987), or Lilwall (1988). This short report however, differs from previous work in that it examines some of the

nonspherically symmetric components of the contained underground explosion. Furthermore, the use of a wavenumber integration algorithm permits us to model the attenuation of the crust in a more exact manner than the modal summation or discrete wavenumber methods used by some earlier workers.

Any nonlinear free-surface interaction must be accompanied by shallow deviatoric sources. Therefore, the relative importance of these secondary nonlinear sources for the excitation of regional phases is important for stable yield estimators as well as for discrimination between earthquakes and explosions. Spall is the simplest nonlinear free-surface interaction that is commonly observed, but by no means are the shallow nonlinear interactions limited to just spall.

When we consider the factors that may cause the explosion source to deviate from spherical symmetry, it is clear that the presence of the free-surface, the vertical gradient in confining stress, and the vertical variation of material properties are the most significant. All of these effects may be considered in a two-dimensional axisymmetric geometry (cylindrical coordinates) where material properties are a function of only depth (z).

For simplicity we restrict ourselves to the study of axisymmetric sources although there is ample evidence that explosions at the Nevada Test Site (NTS) radiate long period Love waves (Toksoz and Kehrer, 1972), long period SH body waves (Wallace, *et al.*, 1985), as well as short period SH body waves (McLaughlin, *et al.*, 1983; Stump and Johnson, 1984; Johnson, 1988). Explosions at the Eastern Kazakhstan Test Site (EKTS) are known to exhibit tectonic

release in long-period surface waves (Day and Stevens, 1986) and recently anomalous SH phases have been observed at regional distances (Priestley, *et al.*, 1990). Although the origins of SH waves from explosions are still under investigation, no researcher has found a consistant correlation between long-period tectonic release and short-period seismic signals. Johnson (1988) found that the non-diagonal parts (non-axisymmetric components) of the moment tensor (0.25-5 Hz) were small and the largest deviation from sphericity was the variation in M_{zz} versus M_{xx} and M_{yy}. It appears that the most important deterministic nonspherical aspects of the explosion source can be characterized by axisymmetric sources.

We consider three generic axisymmetric moment tensor sources ($M_{xx}=M_{yy}$, $M_{xy}=M_{xz}=M_{yz}=0$); the explosion, the compensated linear vector dipole (CLVD), and the horizontally oriented tension crack. The linear combination of any two of these sources will serve to represent any axisymmetric first order moment tensor source. The explosion moment tensor,

$$\begin{bmatrix} M_{xx} & M_{xy} & M_{zx} \\ M_{yx} & M_{yy} & M_{yz} \\ M_{zx} & M_{zy} & M_{zz} \end{bmatrix} = M_I \begin{bmatrix} 1 & 0 & 0 \\ 0 & 1 & 0 \\ 0 & 0 & 1 \end{bmatrix},$$

the CLVD moment tensor,

$$\begin{bmatrix} M_{xx} & M_{xy} & M_{zx} \\ M_{yx} & M_{yy} & M_{yz} \\ M_{zx} & M_{zy} & M_{zz} \end{bmatrix} = M_{CLVD} \begin{bmatrix} -1 & 0 & 0 \\ 0 & -1 & 0 \\ 0 & 0 & 2 \end{bmatrix},$$

and the tension crack,

$$\begin{bmatrix} M_{xx} & M_{xy} & M_{zx} \\ M_{yx} & M_{yy} & M_{yz} \\ M_{zx} & M_{zy} & M_{zz} \end{bmatrix} = \delta\bar{u}A \begin{bmatrix} \lambda & 0 & 0 \\ 0 & \lambda & 0 \\ 0 & 0 & (\lambda+2\mu) \end{bmatrix} = M_{TC} \begin{bmatrix} 1 & 0 & 0 \\ 0 & 1 & 0 \\ 0 & 0 & \frac{\lambda+2\mu}{\lambda} \end{bmatrix},$$

where M_I is the isotropic explosion moment, M_{CLVD} is the CLVD moment, M_{TC} is the tension crack moment, and $\delta\bar{u}$ is the displacement separation across the tension crack with area A. The tension crack has been used as a model for spall (Day, *et al*, 1983), although general axisymmetric nonlinear free-surface interactions may result in more general linear combinations of any of these three generic sources. It is unlikely, however, that any nonlinear deformation would occur that did not exhibit some deviatoric component since the normative failure mode in rocks is shear failure.

For the purposes of computing far-field regional seismograms we use a wavenumber integration algorithm (Apsel and Luco, 1983) that computes the complete P-SV wavefield in an attenuating layered earth model. This method has been found to be superior to modal summation for regional seismogram synthesis when attenuation is a significant aspect of the propagation (Day, *et al.*, 1989).

Several crustal models are considered to give a flavor for the potential variation of regional phase excitation from model to model but the models are not considered to be exhaustive. Tabulations of the models are found at the end of this section in Tables 4.1 through 4.8. Two basic sets of models are considered. First, models with a high free-surface velocity (P-wave velocity > 4000 m/s) are considered. Next some models with low free-surface velocities (P-

wave velocity < 4000 m/s) and hence high velocity gradients in the upper crust are considered. We are concerned with evaluating the relative excitation of Pg and Lg as a function of frequency in the short-period band (0.25 to 5 Hz) for shallow axisymmetric moment tensor sources. An important aspect of many of these models is that attenuation (1/Q) is higher in the upper few kilometers of the crust. This aspect of a model serves to attenuate high frequency Rg and other waves that are confined to the near-surface layers. This is particularly important in models with low near-surface velocities.

High Near-Surface Velocity Models

Lilwall (1988) presented a theoretical analysis of the discrimination between earthquakes and explosions using explosion and earthquake sources located in a crustal structure with an upper 1000 m thick layer of 4000 m/s P-wave velocity. He points out that in such a high P-wave velocity structure that Lg amplitude is largely due to a 'nongeometric' S wave referred to as S*. The curved compressional wavefront from the point explosion source produces a frequency dependent SV reflection that is seen at regional distances as Lg. We examine Lilwall's suggestion that the S* phase is largely responsible for the Lg from shallow explosions. If true, then the low-frequency character of the S* phase would provide a theoretical basis for the discrimination between explosions and earthquakes.

Figure 4.1 shows a suite of Green's functions for explosion sources at depths of 100, 300, 500, 700, 900, 1100 and 1300 meters for a surface vertical

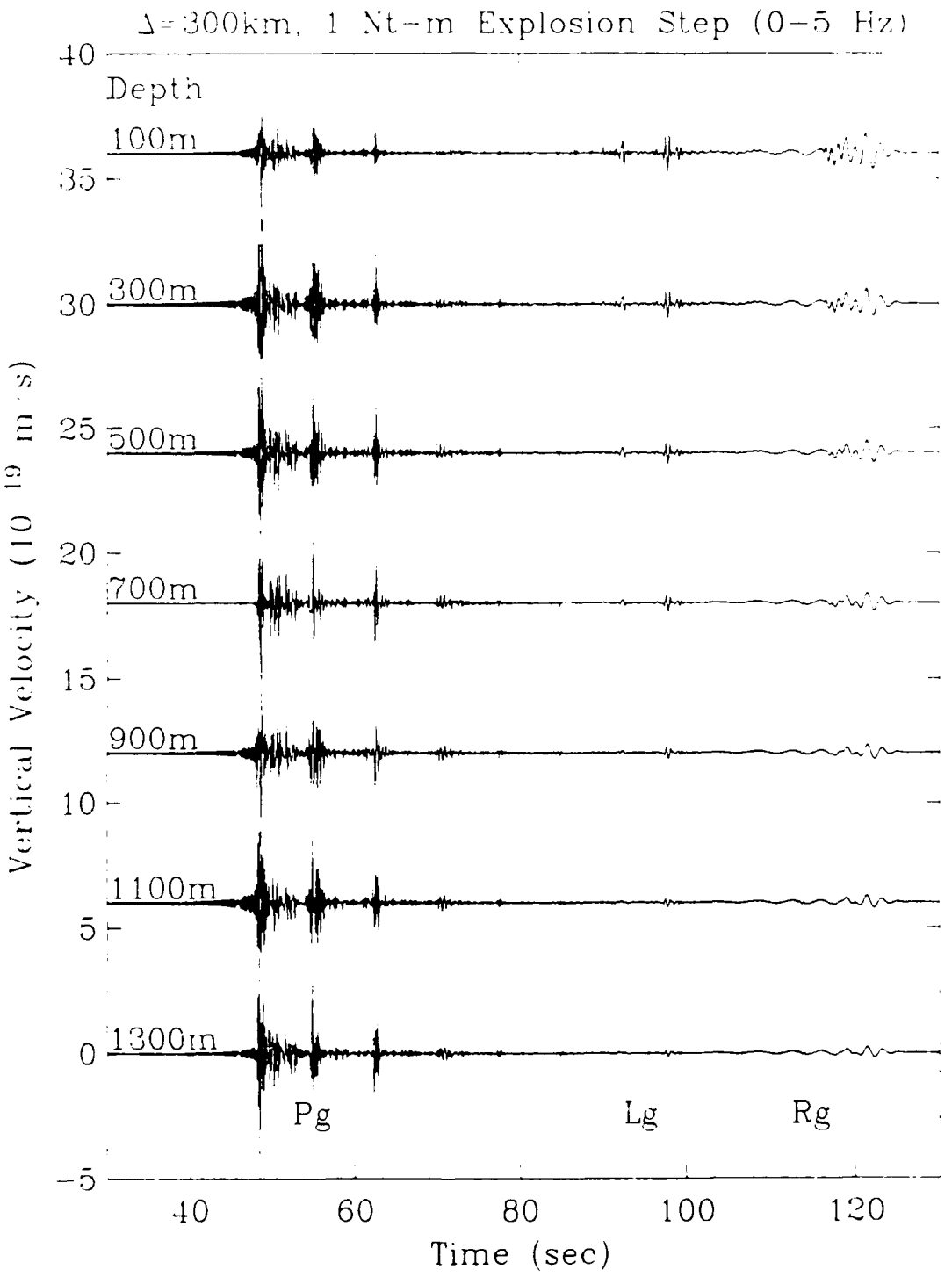

Figure 4.1. Explosion Green's functions (0-5 Hz) at a distance of 300 km for source depths of 100 to 1300 m. Source is a 1 Nt-m step function and vertical velocity is in units of 10^{-19} m/s. Pg, Lg and Rg wavepackets are labeled. Note the decay of the excitation of Lg with increasing depth of the source.

receiver at a range of 300 km. The structure is derived from Stevens (1986) and has a surface P-wave velocity of 5020 m/s. The Green's functions are broadband (0-5 Hz) velocity responses (units of m/s) to a step function explosion source (units of Nt-m). The Pg amplitude is roughly constant modulated by variation in the P+pP interference with depth. The broadband Lg amplitude decreases with depth as expected if the primary source for SV energy were the conversion of a curved P wavefront at the free-surface. The Lg is also frequency dependent. The spectral ratios of Lg/Pg are shown in Figure 4.2 as a function of frequency. At 0.25 Hz, the Lg is larger than the Pg for all depths and larger for the 100 meter source than the 1300 meter deep source. The variance between the 100 and 1300 meter deep sources is never greater than a factor of 5 and is much less clear at frequencies above 2 Hz than below 2 Hz. Note that at 1 Hz, all explosion sources exhibit Lg/Pg ratios less than 1.

At the same scale as Figure 4.1, a suite of tension crack Green's functions for the same source depths are shown in Figure 4.3. For the same moment, the tension crack Pg amplitudes are about 1/2 the explosion Pg amplitudes while the tension crack Lg amplitudes are several times larger than the explosion Lg amplitudes. The deviatoric part of the tension crack source provides a direct source of SV energy to propagate at Lg phase velocities. An investigation of the frequency content of the Lg/Pg ratio shows that the tension crack produces more Lg than an explosion source over a broad bandwidth. The discrepancy is so large that small amounts of a tension crack source will produce Lg comparable to the pure explosion.

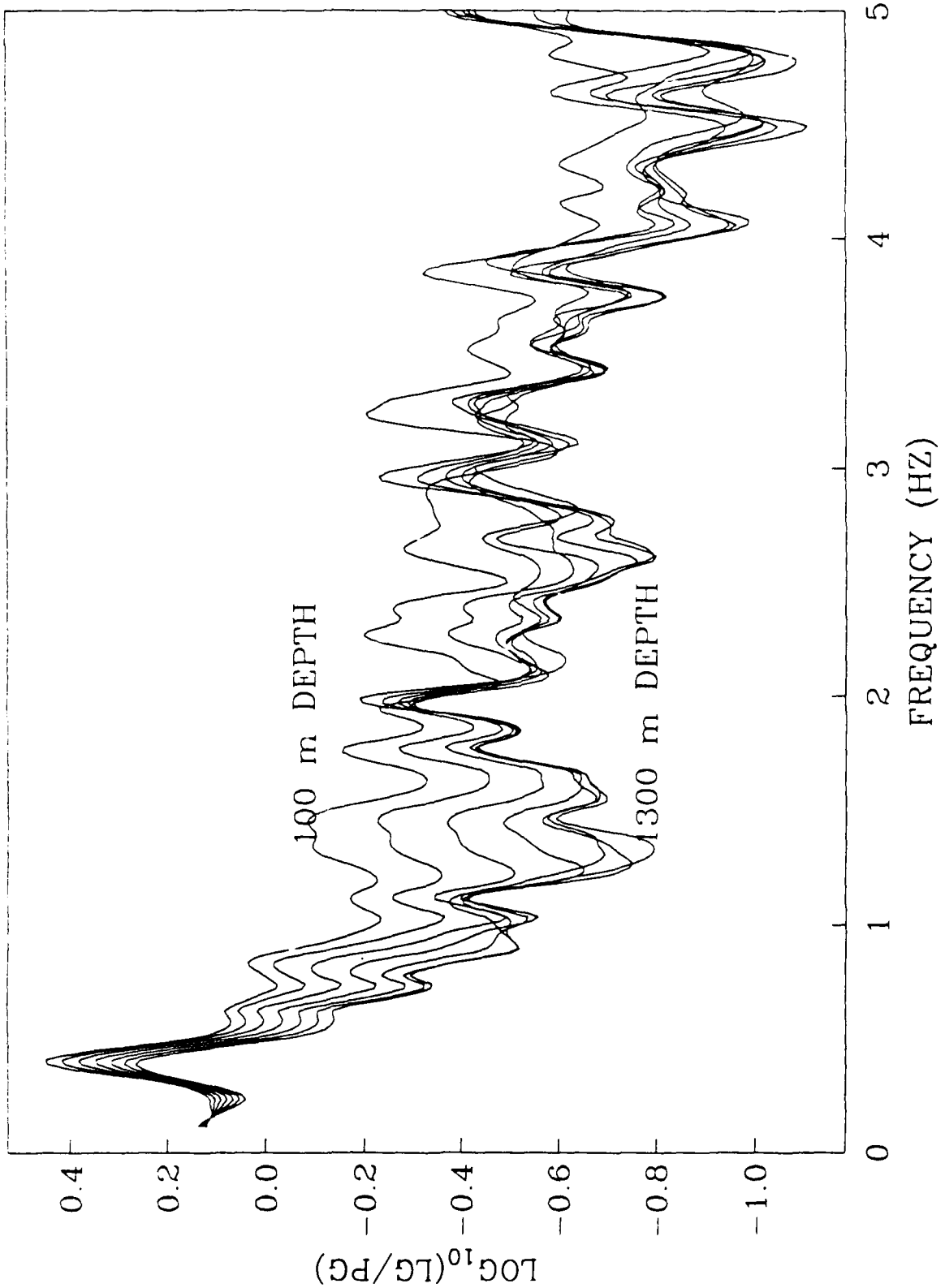

Figure 4.2. Theoretical Lg/Pg ratio as a function of frequency and depth for a point explosion source at Δ = 300 km in a high velocity structure (Stevens, 1986).

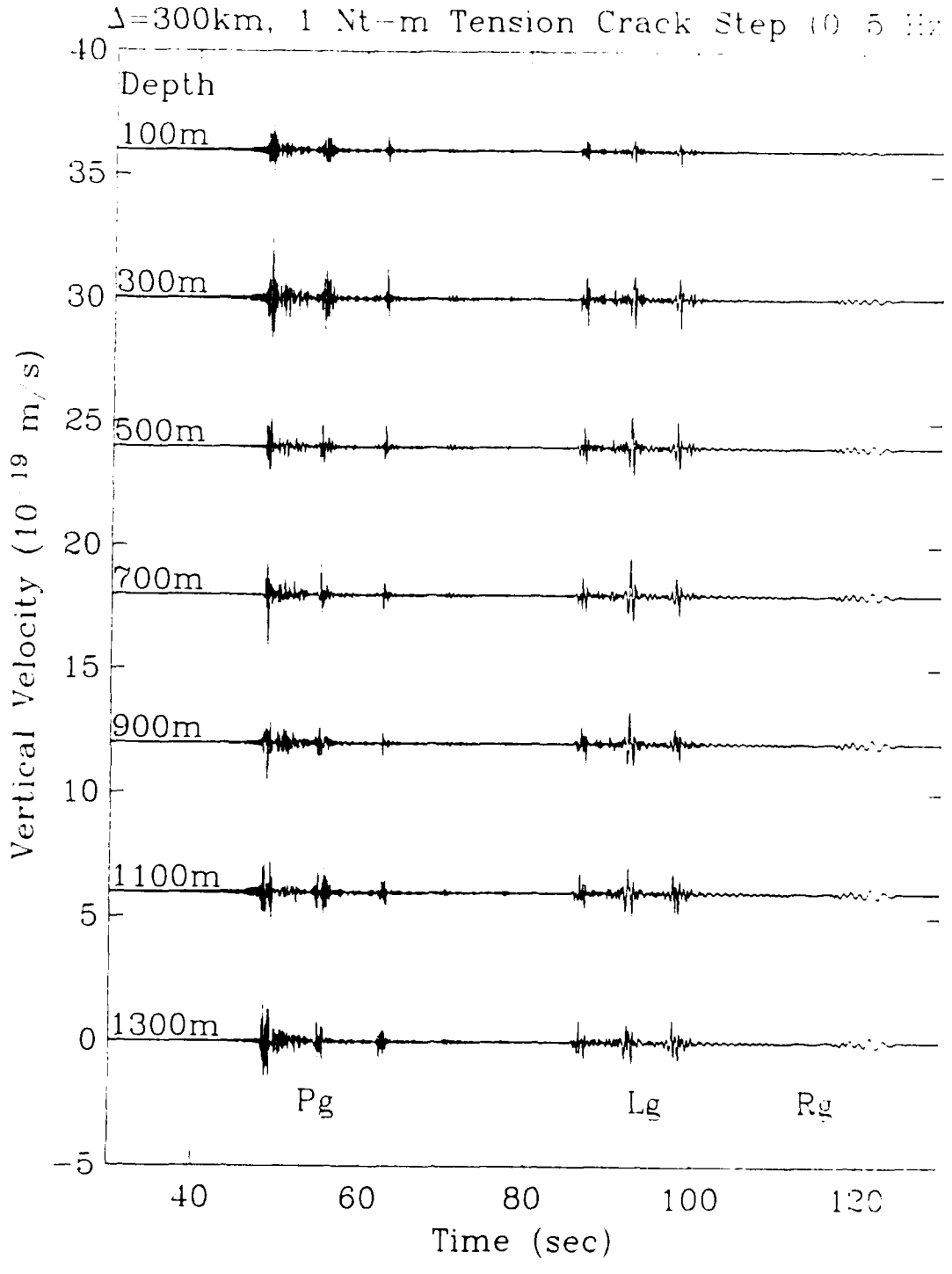

Figure 4.3. Tension crack Green's functions (0-5 Hz) at a distance of 300 km for source depths of 100 to 1300 m. Source is a 1 Nt-m step function and vertical velocity is in units of 10^{-19} m/s. Pg, Lg, and Rg wavepackets are labeled. Note that in comparison to Figure 4.1, the Lg is larger and does not decay with increasing depth of the source.

Figures 4.4 and 4.5 show Green's functions at a receiver distance of 256 km for an explosion and a CLVD source at a depth of 500 meters as computed for a suite of models proposed for the region around the EKTS (see Tables 4.1-4.7). The models have varying crustal thickness, Pn velocities, attenuation, and crustal gradients. Three of the models have crustal low-velocity zones. All models have surface P-wave velocities greater than 5000 m/s. All of the models exhibit very low Lg/Pg levels from the explosion and larger Lg/Pg ratios for the CLVD source. It is clear that these results are not sensitive to the details of the crustal models.

Another way to consider this result is that a 10% asymmetry in the moment tensor source can result in as much Lg as the spherical source would produce. Any nonspherical expansion or spall will result in a CLVD component superimposed on an explosion source. The Lg excited by the deviatoric CLVD source will mask the explosion produced S*.

Low Near-Surface Velocity Models

Crustal models with a low near-surface velocity will invariably have a higher velocity gradient in the upper crust. This low velocity channel traps waves with low phase velocity excited by a shallow source. These low velocity near-surface layers are not contiguous at NTS. However, explosions at NTS initially excite waves in these low velocity layers and the near-source structure determines the character of the energy radiated into the crustal waveguide. To properly treat where this shallow propagating energy goes when these waves

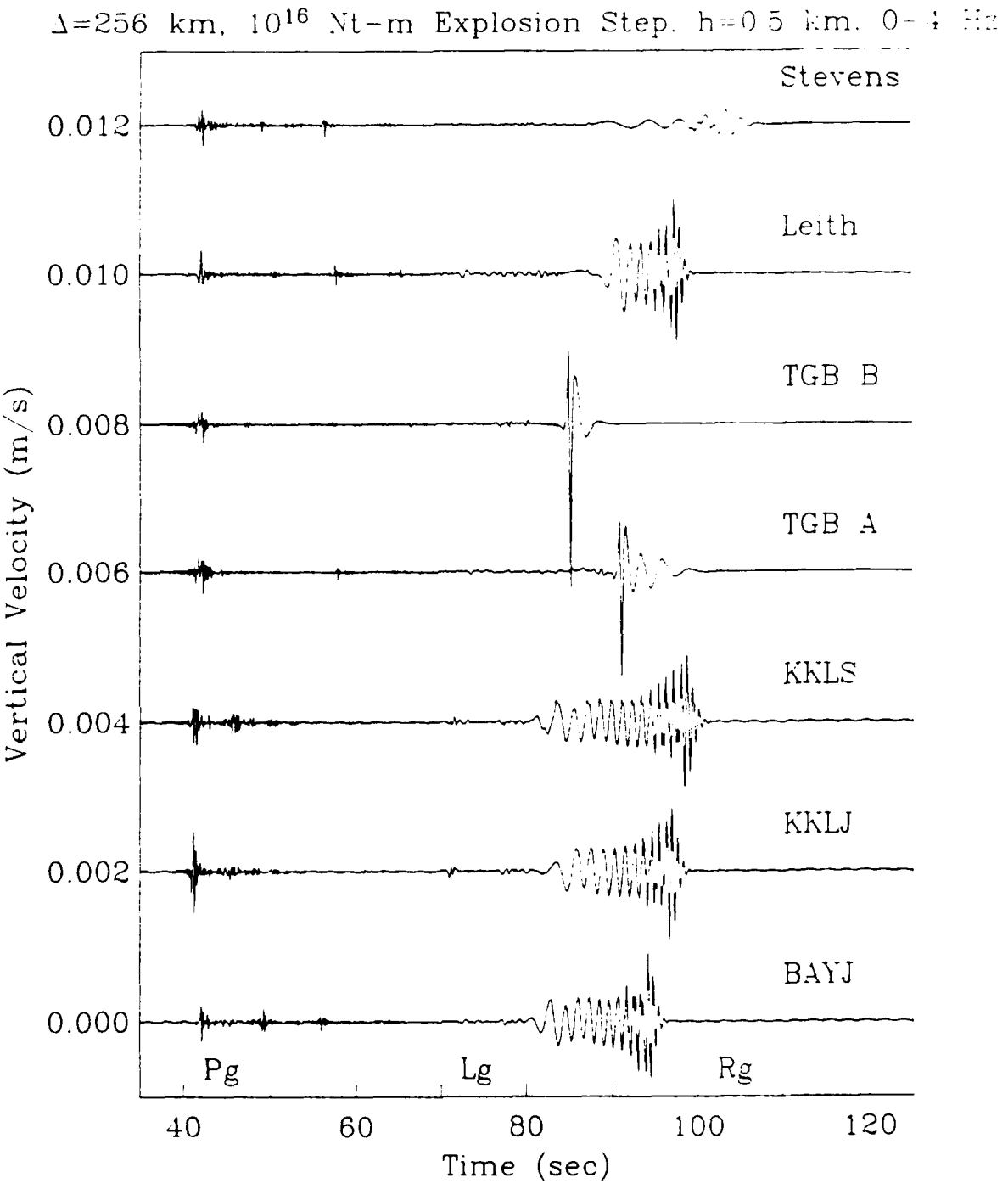

Figure 4.4. Explosion Green's functions (0-4 Hz) at a distance of 256 km for a suite of different crustal structures. The source is at a fixed depth of 500 m. Note the weak Lg excitation for all models. The top model (labeled Stevens) has a low Q layer near the surface that attenuates the high-frequency Rg.

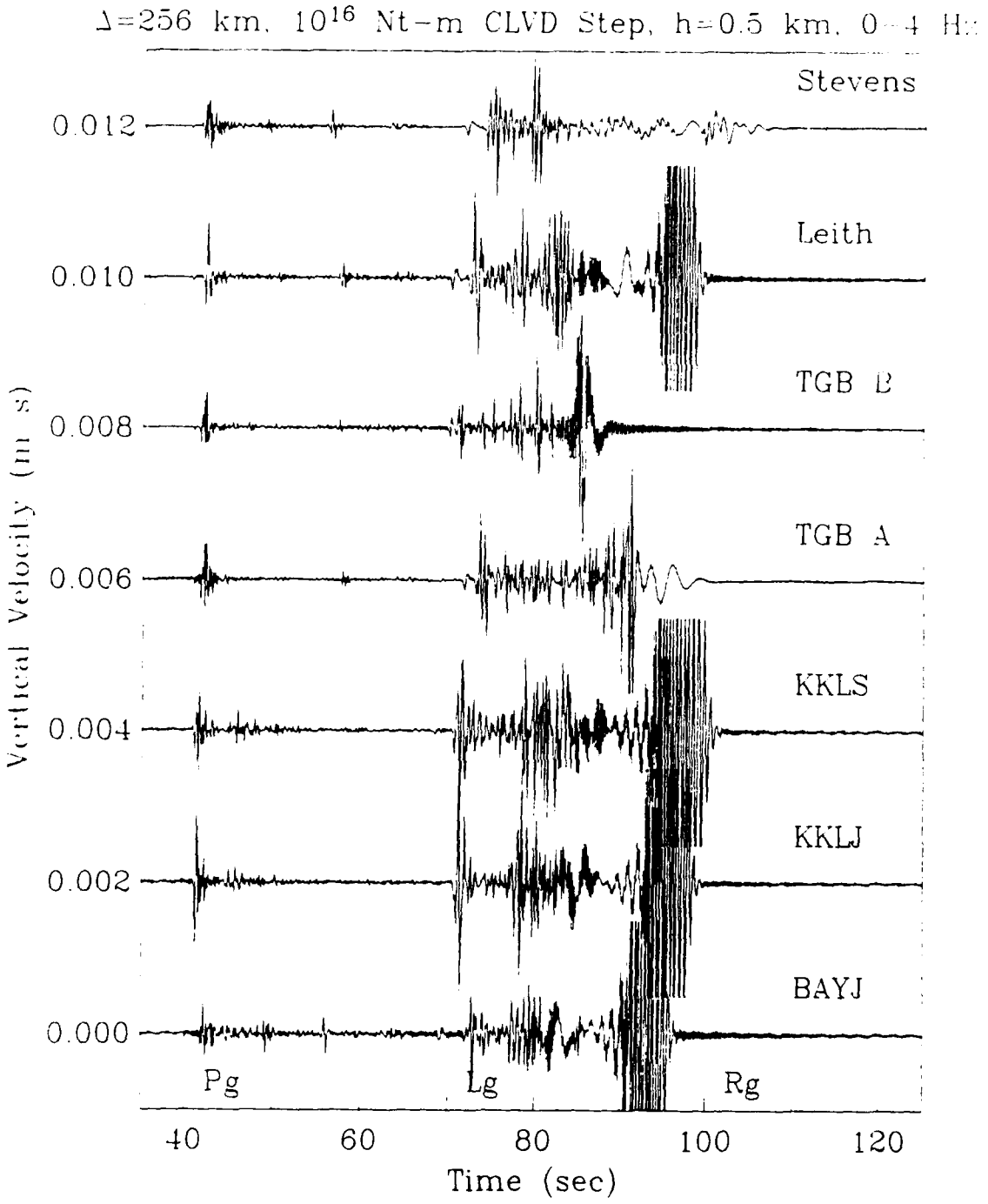

Figure 4.5. CLVD Green's functions (0-4 Hz) at a distance of 256 km for a suite of different crustal structures. The source is at a fixed depth of 500 m. Note the strong Lg excitation for all models. The top model (labeled Stevens) has a low Q layer near the surface that attenuates the high-frequency Rg. Traces have been clipped at +/-0.0015 in order to display them at the same scale as Figure 4.3.

impinge on edges of these low velocity channels is a scattering problem beyond this current work. McLaughlin, *et al.* (1987) suggest that some of this energy is ultimately scattered into the crustal waveguide as Lg, so the analysis presented here may be modified by the scattering hypothesis for the generation of Lg. For the purposes of this report we simply wish to show that the relative Pg and Lg excitation by explosive and CLVD sources in a basin and range structure with low velocity and low Q near-surface layers is quite different from the excitation in the high near-surface velocity models previously discussed.

BR3 (derived from BR2, McLaughlin, *et al.*, 1988) is a layered crustal and upper mantle model with constant Q, designed to fit the propagation of Pn, Pg and Lg waveforms in the 1 Hz bandwidth for explosions at NTS and stations in the basin and range. The model correctly predicts the spatial attenuation of these phases in the regional distance range. At frequencies substantially above 1 Hz, the model progressively fails to model the Lg attenuation properly because apparent Lg Q(f) increases with increasing frequency and BR3 is a constant Q model. BR3 is characterized by low velocity and low Q layers at the surface with velocities and Q increasing with depth. The model was chosen not to optimize the fit for any one path but to represent an average over paths.

Green's functions (0-4 Hz) for a distance of 320 km are shown in Figure 4.6 for explosion and CLVD sources at depths of 250 and 550. In contrast to a similar comparison that is made in Figure 4.4 and 4.5 for the high velocity structure, we see that in the BR3 structure, the CLVD does not excite much more Lg than the explosion. The Eastern Kazakhstan and BR3 models lead to very

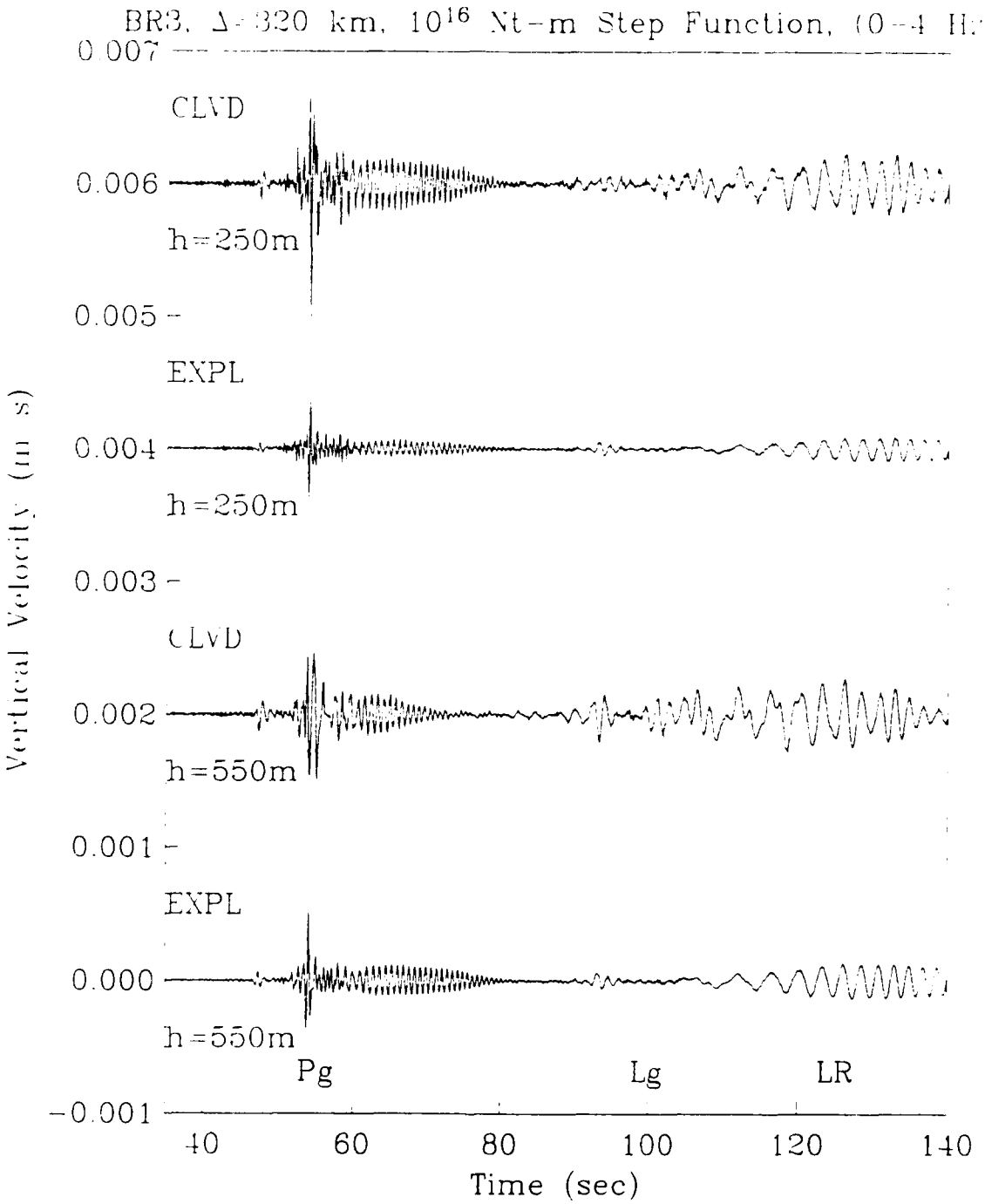

Figure 4.6. Explosion and CLVD Green's functions (0-4 Hz) at a distance of 320 km in the BR3 model. Sources are either 250 or 550 m deep. Note that the peak Lg amplitude from the 250 m CLVD is about the same as the Lg amplitude from the 550 meter explosion. The CLVD sources excite higher-modes that arrive superimposed over the LR.

different conclusions regarding the Lg excitation from CLVD and explosion sources.

In the BR3 model, Lg from the CLVD is more complicated than the Lg from the explosion sources. It appears that the CLVD excites higher modes that interfere with the early portions of the Rayleigh wave. However, the peak Lg amplitude from the CLVD source is not significantly larger than the Lg amplitudes due to the explosion sources. In a structure such as BR3, the CLVD and explosion sources yield similar Lg/Pg ratios. Therefore, in the BR3 structure, the Lg/Pg ratio is invariant with respect to the three generic axisymmetric sources.

Conclusions

The two sets of structures considered, show substantially different relative responses to shallow explosion and CLVD source components. Explosions in structures with near-surface high velocities couple little SV energy into the Lg waveguide while a shallow CLVD component produces much larger SV energy which couples into the Lg waveguide. Consequently the CLVD component of the Lg in the high velocity structure may easily dominate the explosion component of the Lg. In stark contrast, the shallow explosion and CLVD sources in the low velocity structure produce comparable Pg/Lg ratios. It appears that the high attenuation of the near-surface low-Q layer attenuates shear waves trapped in the near-surface layers while the SV energy from the explosion and CLVD components available to the Lg waveguide is more nearly equal in the

low-velocity structure. However, the CLVD Lg signal in the low-velocity structure is more complex presumably because it excites higher modes in the sub 1 Hz frequency band. Patton (1988) has used these higher modes to model the CLVD components of NTS explosions. Because the explosion and CLVD sources produce roughly equal Lg/Pg ratios a procedure similar to Patton's is required to decipher the more complex nature of the source. The indeterminacy of Lg-to-Pg ratios at NTS is demonstrated in Section V of this report using two co-located NTS events recorded at a common station.

It is likely that any underground explosion contains some asymmetries. The simplest first order moment tensor source which models asymmetry in the explosion source is a CLVD. Given the sensitivity of the Lg excitation in a high-velocity crustal structure to the CLVD component it seems unlikely that the observed regional Lg is generated by an explosion S* mechanism. Whether this asymmetry is due to spall or the vertical gradient in the material properties and confining pressure is immaterial to the argument. Since the Lg excitation by a CLVD source is about an order of magnitude greater than by an explosion source, only a 10% CLVD component is required to generate as much Lg as the pure explosion.

Johnson (1988) has found from the inversion of near-field accelerograms at NTS that the M_{zz} component of the moment tensor was out of phase with the M_{xx} and M_{yy} components introducing a CLVD source that was consistent with spall. Patton (1988) examining the same event, HARZER, found similar evidence for the CLVD component of the source while modeling higher-mode

components of the Lg wavetrain. In McLaughlin, *et al.* (1990) (summarized in Section III of this report) we show that the parametric spall models of Barker and Day (1990) (summarized in Section II of this report) predict m_b (Lg) values within reasonable bounds of observation. Whether the axisymmetric asymmetries in the equivalent seismic source are due to spall or other nonlinear processes, it is clear that these nonlinear processes will dominate the excitation of Lg in crustal models with near-surface high velocities.

Given that Lg is known to be a very stable yield estimator, the question arises as to whether asymmetries in the explosion source could be responsible for the reproducible excitation of Lg energy proportional to the yield. Perhaps, for explosions detonated in a fairly uniform brittle material at nearly constant scaled depth, the spall momentum is a good estimate of yield. Other mechanisms also may be at work to stabilize the process of Lg excitation. Scattering of Rg (and shallow P-SV modes) may contribute to the regional Lg signal. Shallow explosions are efficient Rg sources. Rg may be attenuated by scattering as well as by intrinsic attenuation in the upper crust (McLaughlin and Jih, 1987; Jih and McLaughlin, 1988). Since scattering occurs over a large volume of crust there would be a statistical averageing that may stabilize the Lg signal. Untill we have a better understanding of these processes, our understanding of the Lg:yield relation will be unsatisfactory.

Tabulated Crustal Models

The model in Table 4.1 is derived from a model Stevens (1986) based on surface wave studies with some modification due to DSS reports for the region. The Q's have been increased in the crust so the average crustal Q is representative of reported Q's for the region. The model of Leith (1987) was compiled from Soviet literature. The Priestley *et al.* (1988) models are based on teleseismic P-wave receiver functions for the stations BAY and KKL. The models from Thurber, *et al.* (1989) were used to locate quary blasts in the region and are derived to some extent from the Priestley, *et al.* (1988) models. For most models $\beta = \alpha/\sqrt{3}$, and $\rho = 770 + 0.32\ \alpha$. Where Q_μ was not specified, a uniform value of 367 was used as reported by Priestley, *et al.* (1990). Therefore these tabulations represent models actually used in calculations and not necessarily the exact models advocated by the cited authors. Model BR3 is a modified version of BR2 from McLaughlin, *et al.* (1988) with a lower near-surface Q compensated by a higher Q in the lower crust.

Table 4.1. Derived from Stevens (1986)					
h(m)	α(m/s)	β(m/s)	ρ(kg/m^3)	Q_μ	Q_k
2000	5020	2790	2700	100	∞
1000	5400	3000	2700	150	∞
2488	5900	3300	2700	200	∞
10976	6100	3400	2700	600	∞
5488	6308	3541	2702	525	∞
5488	6597	3703	2807	500	∞
5488	6736	3781	2858	450	∞
5564	6782	3807	2875	400	∞
6504	6795	3814	2879	350	∞
8006	8147	4573	3372	179	∞
9359	8138	4568	3369	167	∞
10940	8106	4550	3358	159	∞
12780	8065	4527	3343	153	∞
14950	8047	4517	3336	150	∞
17470	8070	4530	3345	148	∞
20420	8117	4556	3361	148	∞
23880	8154	4577	3375	147	∞
27910	8161	4581	3378	147	∞
32630	8145	4572	3372	146	∞
38140	8120	4558	3363	146	∞
∞	8101	4547	3356	145	∞

Table 4.2. Leith (1987) DSS Model					
h(m)	α(m/s)	β(m/s)	ρ(kg/m^3)	Q_μ	Q_k
1000	5100	2944	2402	367	∞
4000	5600	3233	2562	367	∞
7000	6050	3492	2706	367	∞
12000	6350	3666	2802	367	∞
12000	6600	3810	2882	367	∞
7000	6900	3983	2978	367	∞
7000	7000	4041	3010	367	∞
∞	8350	4820	3442	367	∞

Table 4.3. Priestley, *et al.* (1988) BAY Model J					
h(m)	α(m/s)	β(m/s)	ρ(kg/m^3)	Q_μ	Q_k
1000	5320	3071	2472	367	∞
3000	5960	3441	2677	367	∞
6000	5660	3267	2581	367	∞
5000	6010	3469	2693	367	∞
10000	6290	3631	2782	367	∞
5000	6650	3839	2898	367	∞
15000	6890	3977	2974	367	∞
∞	8330	4809	3435	367	∞

Table 4.4. Preistley, *e al.* (1988) KKL Model J					
h(m)	α(m/s)	β(m/s)	ρ(kg/m^3)	Q_μ	Q_k
1000	5190	2996	2430	367	∞
4000	5850	3377	2642	367	∞
2500	5770	3331	2616	367	∞
2500	5570	3215	2552	367	∞
2500	5900	3406	2658	367	∞
5000	6190	3573	2750	367	∞
10000	6520	3764	2856	367	∞
15000	7040	4064	3022	367	∞
10000	7470	4312	3160	367	∞
5000	7800	4503	3266	367	∞
∞	8100	4676	3362	367	∞

Table 4.5. Priestley, *et al.* (1988) KKL Model S					
h(m)	α(m/s)	β(m/s)	ρ(kg/m^3)	Q_μ	Q_k
1000	5140	2967	2414	367	∞
4000	5910	3412	2661	367	∞
7500	5510	3181	2533	367	∞
2500	6030	3481	2699	367	∞
12500	6510	3758	2853	367	∞
12500	7080	4087	3035	367	∞
2500	7290	4208	3102	367	∞
15000	7490	4324	3166	367	∞
∞	8100	4676	3362	367	∞

Table 4.6. Thurber, Given, and Berger (1989) Model A					
h(m)	α(m/s)	β(m/s)	ρ(kg/m^3)	Q_μ	Q_k
5000	5400	3050	2498	367	∞
5000	6150	3500	2738	367	∞
10000	6350	3600	2802	367	∞
10000	6550	3700	2866	367	∞
10000	6750	3850	2930	367	∞
10000	6950	3950	2994	367	∞
∞	8200	4650	3394	367	∞

Table 4.7. Thurber, Given, and Berger (1989) Model B					
h(m)	α(m/s)	β(m/s)	ρ(kg/m^3)	Q_μ	Q_k
5000	5400	3300	2498	367	∞
5000	6150	3400	2738	367	∞
10000	6350	3500	2802	367	∞
10000	6550	3700	2866	367	∞
10000	6750	4100	2930	367	∞
10000	6950	4300	2994	367	∞
∞	8200	4700	3394	367	∞

Table 4.8. BR3, NTS - Basin & Range Model					
h(m)	α(m/s)	β(m/s)	ρ(kg/m^3)	Q_μ	Q_k
500	3000	1500	2000	50	∞
500	3800	2200	2200	75	∞
2000	5800	3400	2800	125	∞
3000	6000	3460	2900	125	∞
14000	6300	3640	2900	150	∞
4000	6500	3750	2900	150	∞
4000	6800	3930	3000	150	∞
6000	6900	3980	3000	150	∞
4000	7800	4500	3200	200	∞
4000	7840	4500	3200	200	∞
4000	7880	4500	3200	200	∞
4000	7920	4500	3200	200	∞
4000	7960	4500	3200	200	∞
2000	8000	4500	3200	200	∞
4000	8050	4500	3200	200	∞
10000	7900	4400	3200	75	∞
10000	7800	4200	3200	75	∞
20000	7800	4200	3200	75	∞
20000	7900	4500	3200	75	∞
60000	8000	4550	3300	75	∞
∞	8100	4600	3400	150	∞

Section V

An Analysis of Two Co-Located NTS Events with Different Scaled Depths of Burial

It has been suggested that nonlinear free-surface effects, such as spall, may be efficient radiators of SV radiation and hence regional Lg. Nonlinear free-surface effects are expected to scale with depth in such a way that events at greater scaled depth should exhibit less spall and hence excite less SV radiation from spall. Testing such a hypothesis by the comparison of two similar sized events at significantly different scaled depths is difficult at NTS. This is because of the variability of the geologic structure and because coupling is known to vary across the water table at NTS. Large events at normal scaled depth of burial or small events at large scaled depth of burials are usually below the water table while smaller events at normal depth of burial are above the water table. Also, unless two events are close together differences in path effects can make detailed comparisons difficult.

The underground explosions, Buteo and Duryea, were two events detonated in the mid 1960's on Pahute Mesa at quite different scaled depths but virtually the same location (see Table 5.1). The water table at this location was determined to be at a depth of 660 m, so Duryea was placed above the saturated zone in rhyolite while Buteo was placed in saturated tuff. Duryea had an announced yield of 65 KT and was therefore at a scaled depth of 135 $m-KT^{-1/3}$ which is within the usual range of scaled depths for testing at NTS. Buteo was substantially smaller and therefore over buried. As we will see

below, based on the 1 Hz amplitude ratios of Pg and Lg at KN-UT, Buteo was between 20 and 30 times smaller than Duryea and therefore was at a scaled depth of at least 450 $m-KT^{-1/3}$ or deeper. Nuttli (1986) included Duryea ($m_b(Lg)$ = 5.66) with other well coupled events at NTS and found that the Lg excitation from Duryea was consistent with other events in water-saturated rock at NTS. Therefore, although the two events are not of similar size and above and below the water table, the coupling appears to be excellent for both events and they are nearly co-located with a large difference in scaled depth of burial.

Table 5.1. Event Information

Event	Date	O.T.	Lat.	Long.	Depth(m)	Medium
Buteo	12 May 1965	18:15:00.1	37.24	-116.43	696.	tuff
Duryea	14 April 1966	14:13:43.1	37.24	-116.43	544.	rhyolite

Since the two events are virtually at the same location, comparisons of Pg and Lg at a common seismic station can serve to test the hypothesis that variations in scaled depth cause variations in the relative Pg to Lg excitation. Although the different yields imply different explosion sources, the ratios of Lg/Pg from two point explosion sources so close together should be the same recorded at the same regional station. Few on scale recordings of these two events are available at common stations; however, the LRSM station KN-UT (Kanab Utah) at a distance of 321 km did record these two events with good signal-to-noise in the short period band.

KN-UT seismograms are shown for the two events in Figure 5.1. Because highpass filtered records of the two events showed that the Lg above 5 Hz was primarily Pg coda, we use bandpass filtered estimates of the signal strength rather than spectral estimates. In this way, the Lg excitation is only measured if energy can be seen above the coda of the preceding phase. Bandpass filters were applied to the vertical and radial components and the rectified seismogram was smoothed with a 2 second moving average. The peak amplitude of the smoothed envelope was taken as a measure of the excitation of Pg and Lg in each frequency bandpass. The procedure was repeated for radial component of motion. Ratios of Lg/Pg and Lg/Lg were found to be the same using both the vertical and radial components so the results shown are based on the average of the vertical and radial components of motion.

The upper portion of Figure 5.2 shows the ratio of (Duryea Pg)/(Buteo Pg) and (Duryea Lg)/(Buteo Lg). Note that both phases show a systematic decline in the ratio from 0.25 Hz to 5 Hz. At 1 Hz, Duryea is about 20 times larger than Buteo while at 5 Hz, Duryea is only about 5 to 6 times larger than Buteo. This is consistent with Buteo's higher corner frequency since it was a smaller yield and located at a greater depth. The Lg window is dominated by Pg coda above 5 Hz and no Lg/Lg ratios are shown for frequencies above 5 Hz. The (Duryea Lg)/(Duryea Pg) and (Buteo Lg)/(Buteo Pg) ratios are shown in the lower portion of Figure 5.2. The relative excitation of Lg/Pg is quite consistent for the two events up to 5 Hz. Below 1 Hz, the Lg/Pg ratio is about 3 to 2 while above 1 Hz, the Lg/Pg ratio is about 1 to 4 for both events. Upper bounds to the

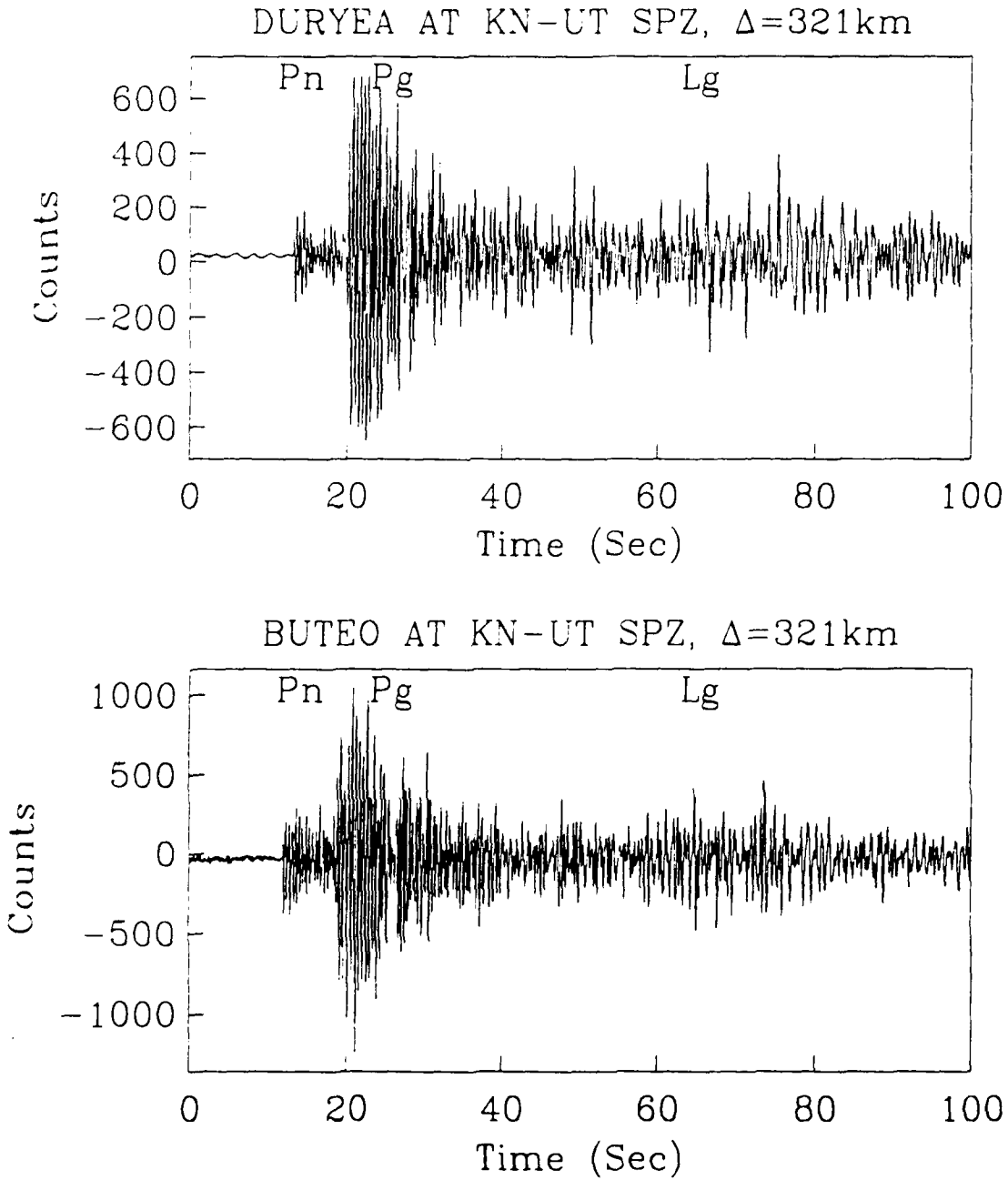

Figure 5.1. Duryea and Buteo recorded on the short period vertical channel at LRSM station KN-UT (Kanab, Utah). Pn, Pg and Lg phases are indicated on the figure. The similarity of the two records is clear with the Buteo exhibiting a somewhat higher frequency signal than Duryea due to source scaling.

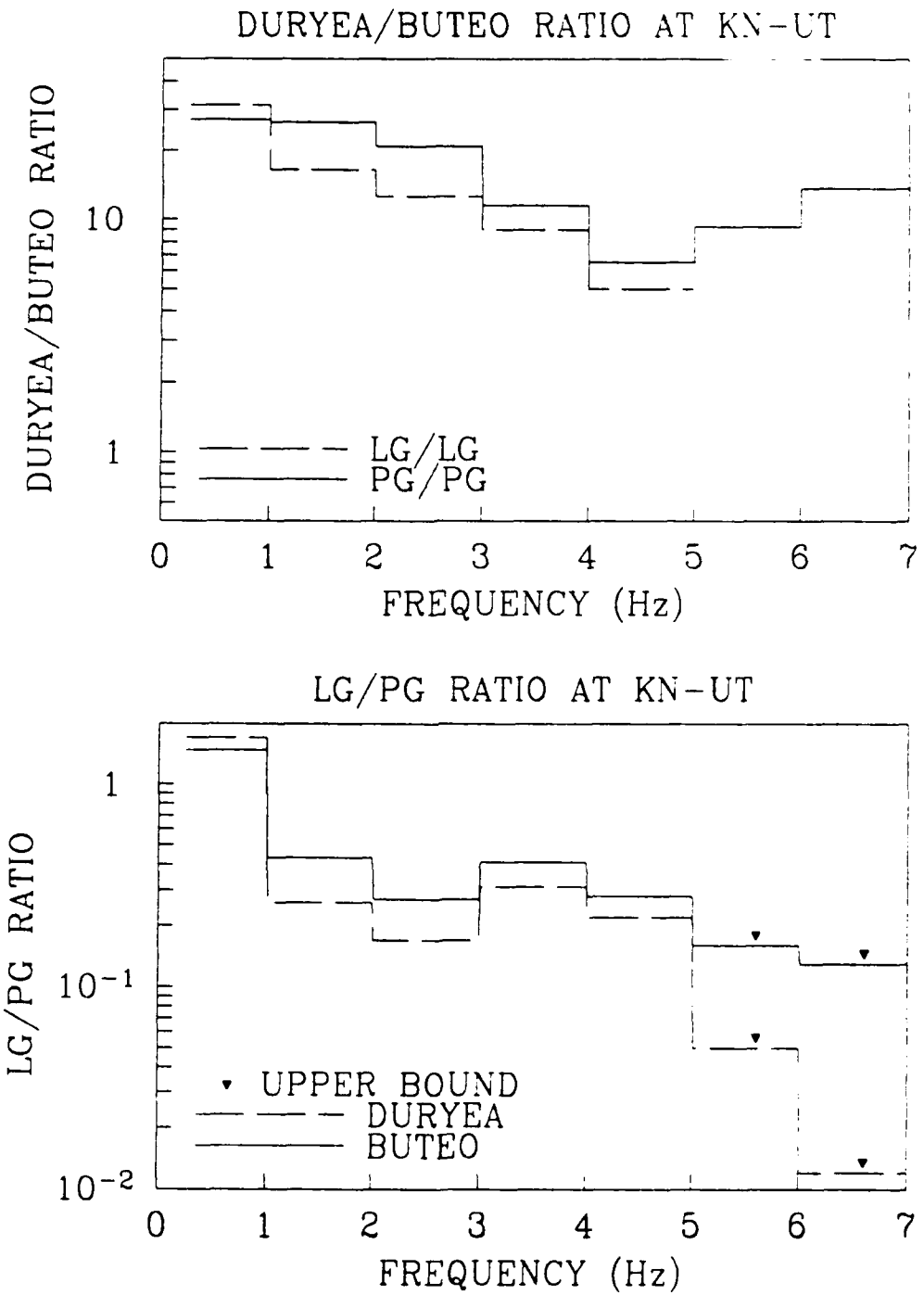

Figure 5.2. Ratios of bandpass filtered KN-UT records of Duryea and Buteo. Above, the ratios of Duryea/Buteo for Pg and Lg. Below, the ratios of Lg/Pg for Duryea and Buteo. The two events have very similar Lg/Pg excitation as a function of frequency. Lg is dominated above 5 Hz and only upper bounds are placed on the Lg/Pg ratios above 5 Hz.

Lg/Pg ratios are indicated above 5 Hz.

This comparison of these two events indicates that although the two events differed in scaled depth by over a factor of 3, the relative Lg and Pg excitation are virtually the same from 0.25 to 5 Hz. The absolute depths of these events differ by less than a 1/4 the S-wave wavelength at 5 Hz (about 2000 m/s). Because the two hypocenters were located so close to each other, the propagation and station effects should cancel, and we must conclude that, apart from the spectral differences due to source scaling, the source mechanisms appear very similar.

In order to better understand the excitation of Lg and Pg for an explosion at NTS propagating in a basin and range crustal structure we have computed reflectivity synthetics for some simple point sources. The basin and range structure, BR3, is taken from McLaughlin, *et al.* (1988). Figure 5.3 shows the response of this structure to point explosions at 250, 550, and 660 meters depth as well as a CLVD source at 250 meters depth. The synthetics are broadband (0 to 2 Hz) vertical velocities from a Heavyside source function with a moment of 10^{16} Nt-m. We model spall by the opening and closing of a tension crack above the explosion source. Such a tension crack source may be represented by the linear combination of the moment tensors for a CLVD and an explosion. Consequently, these synthetics can serve as the fundamental elements needed to model an axial-symmetric source that includes both an explosion and spall.

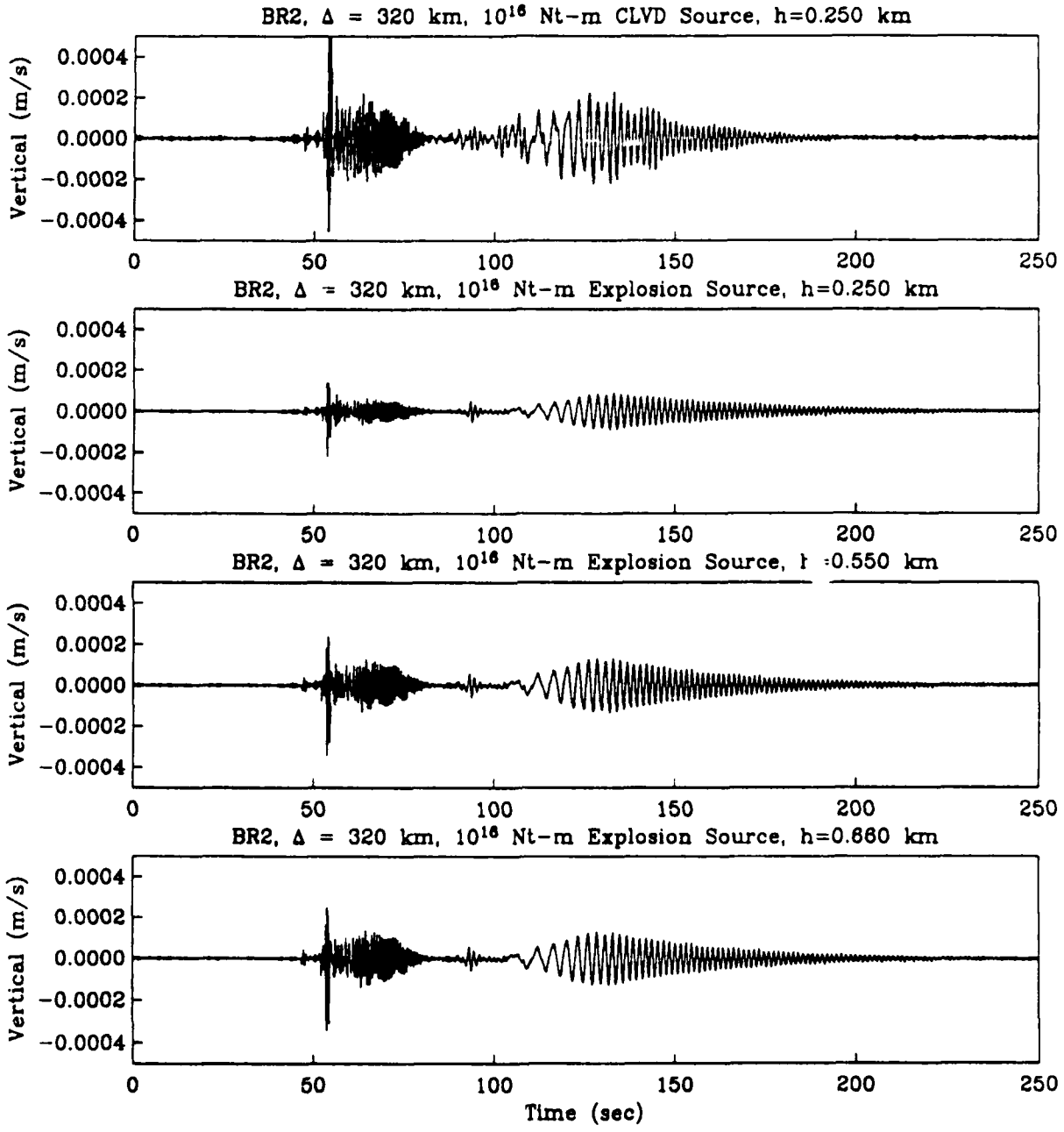

Figure 5.3. Broadband velocity (m/s) synthetics from 0 to 2 Hz for step function sources with moment 10^{16} Nt-m. Top to bottom, a CLVD source at depth of 250 m, an explosion source at depth of 250 m, an explosion source at a depth of 550 m, and an explosion source at a depth of 660 m.

Note that the Pn and Pg amplitudes are roughly the same for the 550 and 660 meter explosion sources and that both of these sources excite a weak and simple Lg pulse that arrives at around 90 seconds. The CLVD source excites a somewhat stronger Pg and a more complicated Lg that lasts longer and interferes with the early portion of the Rayleigh wave. In this layered seismic structure, the CLVD source excites Lg somewhat more efficiently than the explosion but also generates substantial Pg. Therefore, the peak Pg/Lg ratio is not greatly different for the explosion and CLVD source for this structure. Figure 5.4 shows the theoretical Lg/Pg ratios for a vertical receiver at a distance of 320 km from three sources; an explosion at 540 meters depth, an explosion at 250 meters depth, and a CLVD at 250 meters depth. The Lg/Pg ratios were derived by the same procedure as those shown in Figure 5.2. Note that one can not discriminate between the three sources based on the Lg/Pg ratio.

This theoretical result is in stark contrast to the relative excitation of Lg by CLVD and explosion sources in structures with high surface velocities (see Section IV of this report). Explosions in structures with high near surface P-wave velocities excite a small amount of Lg when compared to deviatoric sources such as a CLVD or tension crack source. CLVD and explosion sources in structures with low near surface P-wave velocities like those at NTS produce more nearly comparable Pg/Lg ratios. It appears that the additional shear wave energy radiated by the CLVD is trapped near the surface by the shallow velocity gradients. These near surface layers are more attenuative and the Lg is therefore weaker. Consequently, we conclude that the Duryea-Buteo test is not

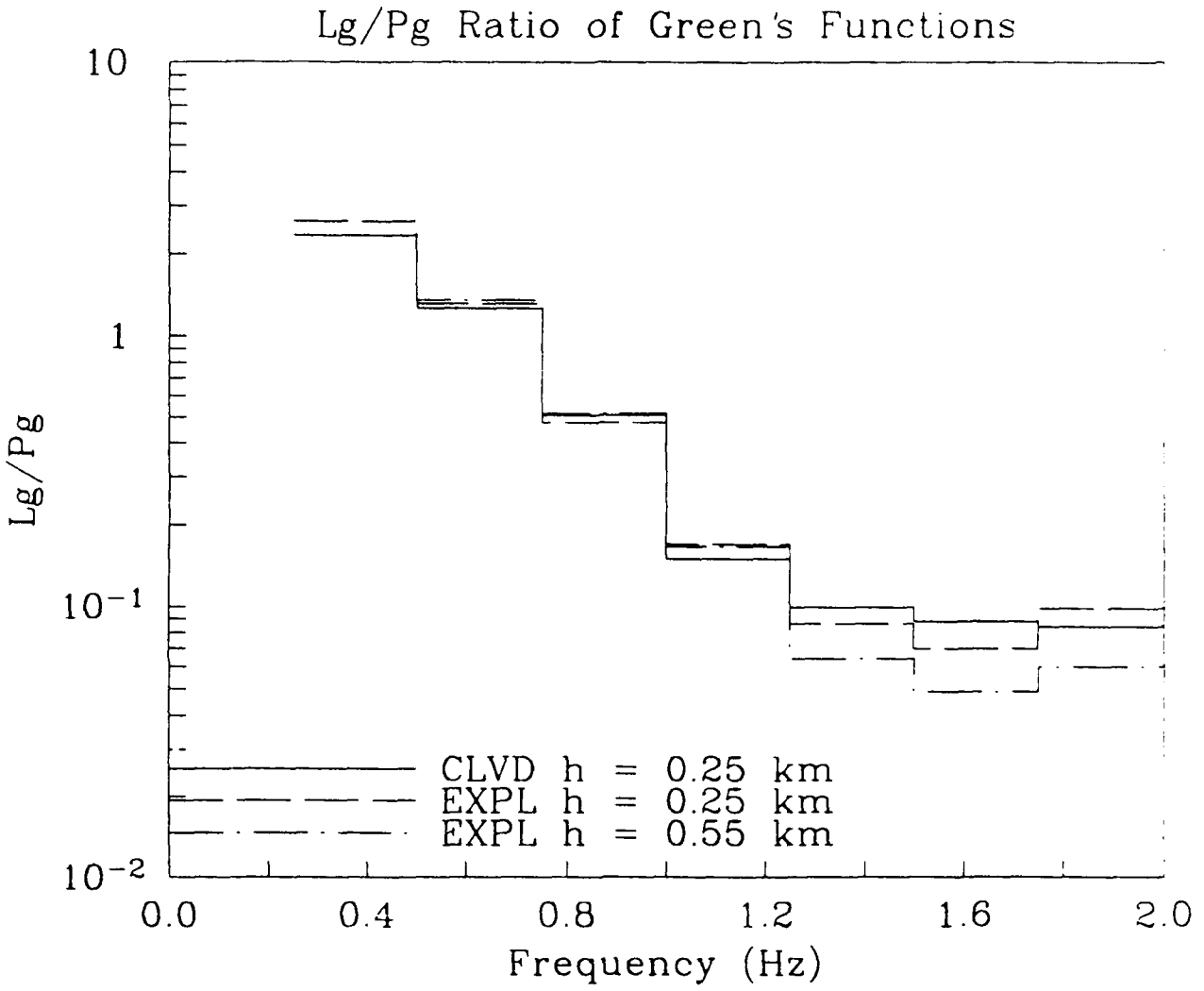

Figure 5.4. Lg/Pg ratios for a vertical receiver distance of 320 km as a function of frequency for three Green's functions; an explosion at 550 meter depth, an explosion at 250 meter depth. The Lg/Pg ratios were derived by the same procedures used to measure Lg/Pg and Pg/Pg ratios in Figure 5.2. All three sources have virtually the same relative excitation of Lg-to-Pg. The frequency dependence of the Lg/Pg ratio is largely due to the differential attenuation between the two phases. It is not possible to discriminate between the three sources based on the Lg/Pg ratios alone.

sensitive to the differential excitation of Pg/Lg as required to test the hypothesis that spall is a significant source of Lg at NTS. Duryea may have exhibited more spall than Buteo but theoretically the Pg/Lg ratios in the short-period band will not serve as a useful discriminant to test this hypothesis.

Section VI

Research in Progress

In this section, we describe two other areas of research that are in progress: scale dependent damage mechanics and finite difference modeling of the Salmon salt dome.

Damage Mechanics

Sammis and Ashby (1988) and Sammis (1989) have derived a model for damage mechanics that is fundamentally scale dependent. The strength of the material depends on the size of cracks within the material and the amount of damage that has been done to the material. The significance of this is that laboratory measurements of rock strength, both measured directly and inferred from small scale explosive tests, all show significantly higher rock strength than that derived from near field measurements of *in situ* rock. One explanation for this phenomenon is that *in situ* cracks are much larger than cracks in small scale experiments, so *in situ* rock on a scale appropriate for underground nuclear explosions may be fundamentally weaker than laboratory scale rock. The damage mechanics model provides a physical mechanism with parameters that scale to the appropriate size to theoretically simulate both laboratory and full scale experiments.

The basic relation for material strength for this model is Equation (28) from Sammis and Ashby (1988), which gives the damage as a function of stress

state. This relation can be reformulated as a function of shear stress, normal stress, and damage. The function then has the form:

$$(S_1 - S_3) = F_1(D)\,(S_1 + S_3) + F_2(D) \tag{1}$$

where S_1, S_3 are the two normalized stress components, D is the damage, and F_1 and F_2 are functions given by:

$$F_1 = \frac{Y - Z}{Y + Z} \tag{2}$$

$$F_2 = \frac{2X}{Z + YZ} \tag{3}$$

where

$$X = C_2 \left[W + \frac{\beta}{\alpha} \right]^{\frac{3}{2}} \tag{4}$$

$$Z = 1 + C_3 \frac{D_0^{\frac{2}{3}}}{1 - D^{\frac{2}{3}}} W^2 \tag{5}$$

$$Y = C_1 Z + C_4 W^2 \tag{6}$$

$$W = \left[\frac{D}{D_0} \right]^{\frac{1}{3}} - 1 \tag{7}$$

and

$$C_1 = \frac{(1 + \mu^2)^{\frac{1}{2}} + \mu}{(1 + \mu^2)^{\frac{1}{2}} - \mu} \tag{8}$$

$$C_2 = \pi\alpha \left[3\frac{\alpha}{\beta} \right]^{\frac{1}{2}} \left[(1 + \mu^2)^{\frac{1}{2}} - \mu \right]^{-1} \tag{9}$$

$$C_3 = 2 \tag{10}$$

$$C_4 = 2\pi\alpha^2 \left[\frac{3}{\beta}\right]^{\frac{1}{2}} \left[(1+\mu^2)^{\frac{1}{2}} - \mu\right]^{-1} \tag{11}$$

where μ is the coefficient of friction, D_0 is the initial damage, and α and β are empirical constants equal to approximately 0.7 and 0.45. The damage, D, is defined by

$$D = \frac{4}{3}\pi (l+\alpha a)^3 N_v \tag{12}$$

where a is the radius of the initial cracks, l is the tensile crack length, and N_v is the crack density. The normalized stresses are defined by

$$S_i = \frac{\sigma_i (\pi a)^{\frac{1}{2}}}{K_I} \tag{13}$$

where K_I is the stress intensity factor at which the tensile cracks grow and σ_i are the stress components.

Equation (1) gives the shear stress at which an increase in crack growth (damage) occurs. This can be implemented within S-CUBED finite difference codes by checking at each step in the calculation to see if the shear stress calculated from an elastic strain increment is below the shear stress obtained from Equation (1) given the normal stress and the previous damage in the cell. If the elastic shear stress exceeds this value, then inelastic strain occurs, causing both an increase in the amount of damage and a decrease in the shear stress. An additional constraint is required to determine how much damage occurs on each strain increment. This constraint can be derived by relating the change in damage to the energy required to increase the crack strain.

Simulation of Seismic Radiation from the Tatum Salt Dome

A second area of continuing research is modeling the seismic radiation from the Salmon explosion using an axisymmetric, linear calculation of an explosion in a salt dome. The purpose of this research is to estimate the amount of Lg generated by scattering from a complex earth structure. Salmon was well recorded and showed strong Lg signals. Furthermore, the earth structure near the source (Tatum salt dome) is fairly well established. It consists of a high velocity salt diapir in low velocity sediments so it contains very high velocity contrasts. This explosion therefore provides an ideal case study for this question.

In Figure 6.1, we show the model that we are using in the calculations for the salt dome structure. The compressional velocity at the source is 4500 meters/second. There is a high velocity region above the source (anhydrite), very low velocity sediments at the surface, and variable velocities gradually increasing with depth outside the salt dome. In Figure 6.2, we show a seismogram from an explosion in this structure at a distance of 16 km. The seismogram was generated using the two-dimensional linear, finite difference code TRES-2D. Figure 6.2 compares the broadband (0-3Hz) seismogram from an explosion (depth 850 m) in the 2D structure with that of an explosion in the 1D layered structure. The difference between these 2D and 1D seismograms is between 10 and 20% of the 2D seismogram in this bandwidth.

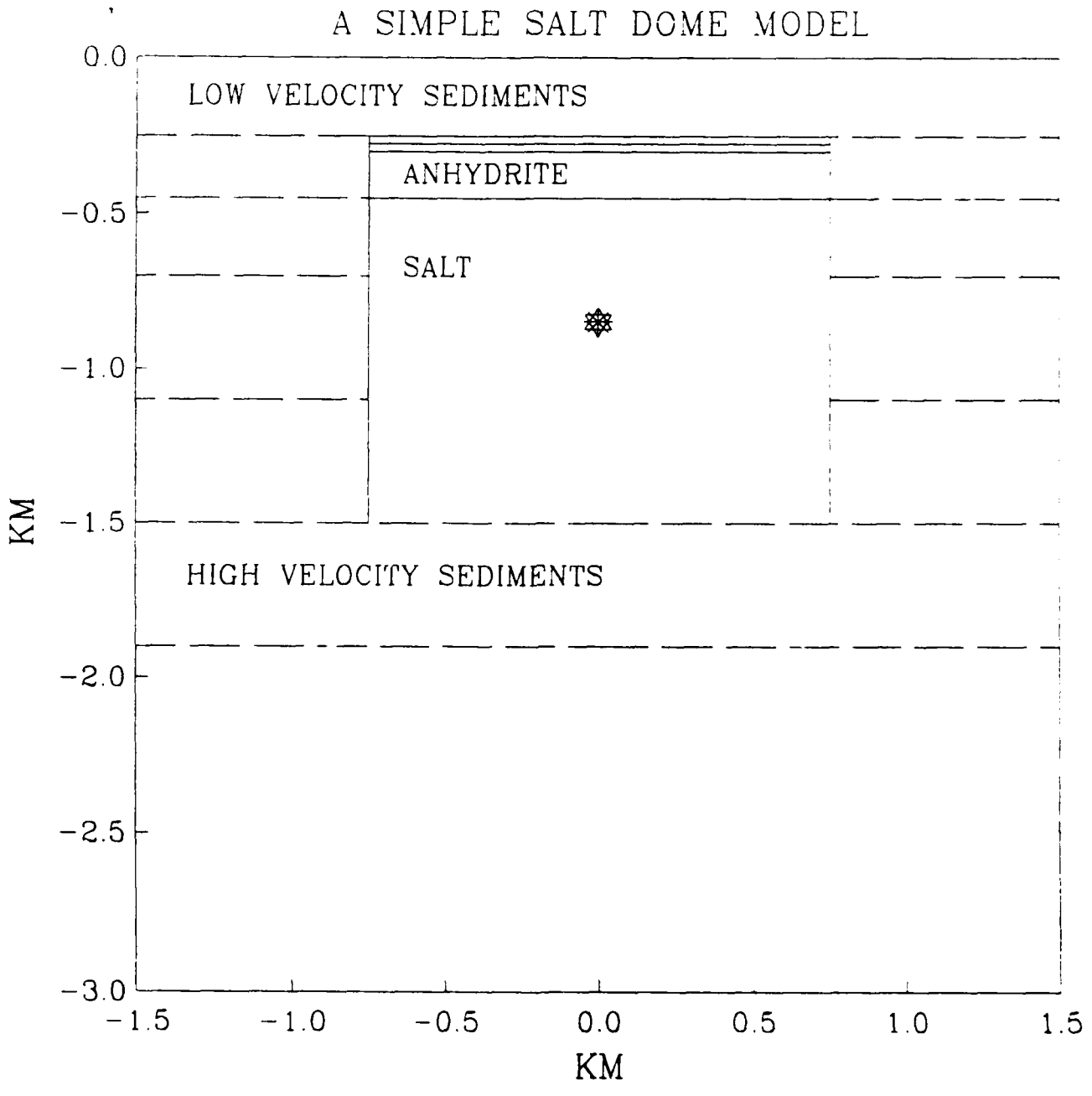

Figure 6.1. Model used for two-dimensional axisymmetric modeling of the Salmon explosion. The P-wave velocity at the source is 4500 m/s. The velocity of the anhydrite layer is 5800 m/s. The velocity of the sediments range from 1900 m/s at the surface to 5000 m/s at the bottom of the grid.

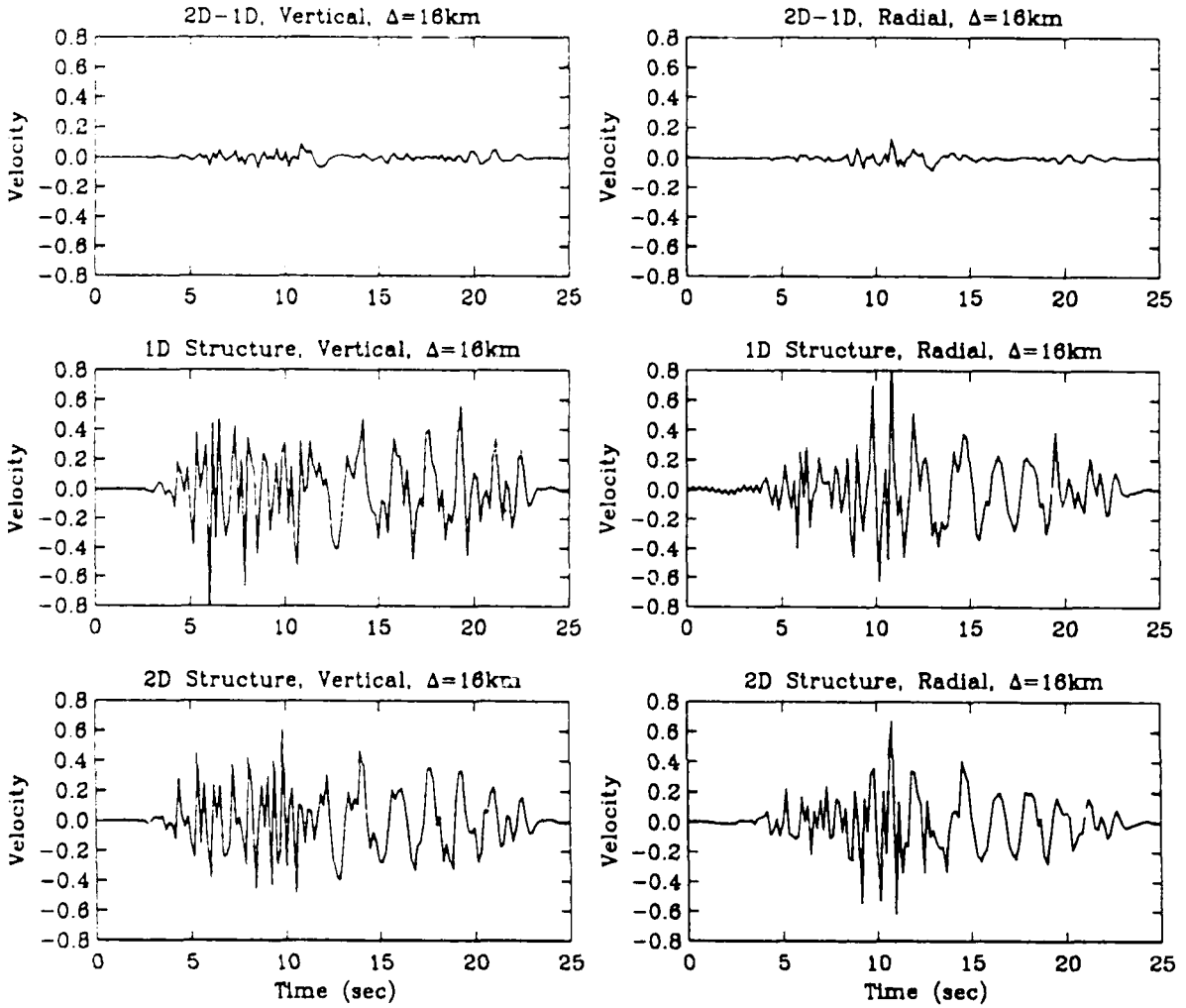

Figure 6.2. Vertical (left) and radial (right) 0-3Hz velocity seismograms at a distance of 16 km for an explosion (depth 850 m) in the 2D structure of Figure 6.1 (bottom) compared to an explosion in a layered structure (middle). The difference between the 1D layered structure and the 2D structure is shown at the top. The 2D-1D difference seismogram is about 10 to 20% of the 2D seismogram.

VII. REFERENCES

Aki, K., P. G. Richards (1980), *Quantitative Seismology, Theory and Methods Volume I,* Freeman, San Francisco.

Apsel, R. J. and J. E. Luco (1983), "On the Green's Functions for a Layered Half-Space, Part II," *Bull. Seism. Soc. Am., 73,* pp. 931-951.

Barker, T. G. and S. M. Day (1990), "A Simple Physical Model for Spall from Nuclear Explosions Based Upon Two-Dimensional Nonlinear Numerical Simulations," Scientific Report No. 3 submitted to the Air Force Geophysics Laboratory, SSS-TR-90-11550, May.

Bennett, T. J., J. R. Murphy and H. K. Shah (1987), "Theoretical Analysis of Regional Phase Behavior," S-CUBED Technical Report submitted to the Defense Advanced Research Projects Agency, SSS-R-87-8113, July.

Campillo, M., M. Bouchon and B. Massinon (1984), "Theoretical Study of the Excitation, Spectral Characteristics, and Geometrical Attenuation of Regional Seismic Phases," *Bull. Seism. Soc. Am., 74,* pp. 79-90.

Day, S. M., N. Rimer and J. T. Cherry (1983), "Surface Waves from Underground Explosions with Spall: Analysis of Elastic and Nonlinear Source Models," *Bull. Seism. Soc. Am., 73,* pp. 247-264.

Day, S. M., N. Rimer, T. G. Barker, E. J. Halda and B. Shkoller (1986), "Numerical Study of Depth of Burial Effects on the Seismic Signature of Underground Explosions," S-CUBED Report to the Defense Nuclear Agency, DNA-TR-86-114, SSS-R-86-7398.

Day, S. M. and J. L. Stevens (1986), "An Explanation for Apparent Time Delays in Phase-Reversed Rayleigh Waves from Underground Nuclear Explosions," *Geophys. Res. Lett., 13,* pp. 1423-1425.

Day, S. M., K. L. McLaughlin, B. Shkoller and J. L. Stevens (1989), "Potential Errors in Locked Model Synthetics for Anelastic Earth Models," *Geophys. Res. Lett., 165,* pp. 203-206.

Eisler, J. D. and F. Chilton (1964), "Spalling of the Earth's Surface by Underground Nuclear Explosions," *J. Geophys. Res., 69,* pp. 5285-5293.

Jih, R. S. and K. L. McLaughlin (1988), "Finite-Difference Modeling of Rayleigh Wave Scattering and P-SV(Lg) Coupling Problems," Air Force Geophysics Laboratory Report, AFGL-TR-88-0093, ADA203221.

Lilwall, R. C. (1988), "Regional m_b:M_S, Lg/Pg Amplitude Ratios and Lg Spectral Ratios as Criteria for Distinguishing Between Earthquakes and Explosions: A Theoretical Study," *Geophysical Journal, 93,* pp. 137-147.

McLaughlin, K. L., L. R. Johnson and T. V. McEvilly (1983), "Two-Dimensional Array Measurements of Near-Source Ground Accelerations," *Bull. Seism. Soc. Am., 73,* pp. 349-375.

McLaughlin, L. M. Anderson and A. C. Lees (1987), "Effects of Local Geological Structure on Yucca Flats, Nevada Test Site, Explosion Waveforms: Two-Dimensional Linear Finite-Difference Simulations," *Bull. Seism. Soc. Am., 77,* pp. 1211-1222.

McLaughlin, K. L. and R. S. Jih (1987), "Finite-Difference Simulations of Rayleigh-Wave Scattering by Shallow Heterogeneity," Air Force Geophysics Laboratory Report, AFGL-TR-87-0322, ADA194961.

McLaughlin, K. L., T. G. Barker, S. M. Day, B. Shkoller and J. L. Stevens (1988), "Effects of Depth of Burial and Tectonic Release on Regional and Teleseismic Explosion Waveforms," AFGL-TR-88-0314, ADA207541, S-CUBED Report SSS-R-88-9844, November.

McLaughlin, K. L., T. G. Barker, and S. M. Day (1990), "Implications of Explosion Generated Spall Models: Regional Seismic Signals," S-CUBED Scientific Report No. 2 submitted to the Air Force Geophysics Laboratory, GL-TR-90-0133, SSS-TR-90-11535, May.

Murphy, J. R. and T. J. Bennett (1983), "A Discrimination Analysis of Short-Period Regional Seismic Data at Tonto Forest Observatory," *Bull. Seism. Soc. Am., 72,* pp. 1351-1366.

Nuttli, O. W. (1986), "Yield Estimates of Nevada Test Site Explosions Obtained from Lg Waves," *JGR, 91,* pp. 2137-2151.

Patton, H. J. (1988), "Source Models of the Harzer Explosion from Regional Observations of Fundamental-Mode and Higher Mode Surface Waves," *Bull. Seism. Soc. Am., 78,* pp. 1133-1158.

Patton, H. J. (1990), "Estimates of Spall Mass and Spall Impulse from Observed Strong Motion Ground Motions on Pahute Mesa," submitted to the *Bull. Seism. Soc. Am.*

Rawson, G. (1988), "How In-Situ Stress, Induced Stress, Fracturing and Spall Might Affect Critical Depths for Explosion Containment and Cratering," Lawrence Livermore National Laboratory Report No. UCID-21461.

Sammis, C. G. and M. F. Ashby (1988), "The Damage Mechanics of Brittle Solids in Compression," Scientific Report No. 1 submitted ot Air Force Geophysics Laboratory, AFGL-TR-88-0160, ADA201653, July.

Sammis, C. G. (1989), "Seismic Pulse Broadening Associated with Fracture Damage Caused by Explosions in Crystalline Rock," Final Report submitted to Air Force Geophysics Laboratory, GL-TR-87-0161, ADA206135, August.

Sobel, P. A. (1978), "The Effect of Spall on m_b and M_S," Teledyne Geotech Report, SDAC-TR-77-12, Dallas, Texas.

Stump, B. W. (1984), "Resolving Point and Couples Forces in Explosion Modeling," (Abstract), *EOS, 65,* pp. 995.

Stump, B. W. and L. R. Johnson (1984), "Near-Field Source Characteristics of Contained Nuclear Explosions in Tuff," *Bull. Seism. Soc. Am., 74,* pp. 1-26.

Stump, B. W. (1985), "Constraints on Explosive Sources with Spall from Near-Source Waveforms," *Bull. Seism. Soc. Am., 75,* pp. 361-378.

Taylor, S. R., N. W. Sherman and M. D. Denny, "Spectral Discrimination Between NTS Explosions and Western United States Earthquakes at Regional Distances," *Bull. Seism. Soc. Am., 78,* pp. 1563-1579.

Taylor, S. R. and G. E. Randall (1989), "The Effects of Spall on Regional Seismograms," *Geophys. Res. Letters, 16,* pp. 211-214.

Toksoz, M. N. and H. H. Kehrer (1972), "Tectonic Strain Release by Underground Nuclear Explosions and its Effect on Seismic Discrimination," *Geophys. J. Roy. astr. Soc., 31,* pp. 141-161.

Viecelli, J. A. (1973), "Spallation and the Generation of Surface Waves by an Underground Explosion," *J. Geophys. Res., 78,* pp. 2475-2487.

Wallace, T. C., D. V. Helmberger and G. R. Engen (1983), "Evidence of Tectonic Release from Underground Nuclear Explosions in Long-Period S Waves, *Bull. Seism. Soc. Am., 75,* pp. 157-174.

Prof. Thomas Ahrens
Seismological Lab, 252-21
Division of Geological & Planetary Sciences
California Institute of Technology
Pasadena, CA 91125

Prof. Charles B. Archambeau
CIRES
University of Colorado
Boulder, CO 80309

Dr. Thomas C. Bache, Jr.
Science Applications Int'l Corp.
10260 Campus Point Drive
San Diego, CA 92121 (2 copies)

Prof. Muawia Barazangi
Institute for the Study of the Continent
Cornell University
Ithaca, NY 14853

Dr. Douglas R. Baumgardt
ENSCO, Inc
5400 Port Royal Road
Springfield, VA 22151-2388

Prof. Jonathan Berger
IGPP, A-025
Scripps Institution of Oceanography
University of California, San Diego
La Jolla, CA 92093

Dr. Lawrence J. Burdick
Woodward-Clyde Consultants
566 El Dorado Street
Pasadena, CA 91109-3245

Dr. Karl Coyner
New England Research, Inc.
76 Olcott Drive
White River Junction, VT 05001

Prof. Vernon F. Cormier
Department of Geology & Geophysics
U-45, Room 207
The University of Connecticut
Storrs, CT 06268

Professor Anton W. Dainty
Earth Resources Laboratory
Massachusetts Institute of Technology
42 Carleton Street
Cambridge, MA 02142

Prof. Steven Day
Department of Geological Sciences
San Diego State University
San Diego, CA 92182

Dr. Zoltan A. Der
ENSCO, Inc.
5400 Port Royal Road
Springfield, VA 22151-2388

Prof. John Ferguson
Center for Lithospheric Studies
The University of Texas at Dallas
P.O. Box 830688
Richardson, TX 75083-0688

Prof. Stanley Flatte
Applied Sciences Building
University of California
Santa Cruz, CA 95064

Dr. Alexander Florence
SRI International
333 Ravenswood Avenue
Menlo Park, CA 94025-3493

Prof. Henry L. Gray
Vice Provost and Dean
Department of Statistical Sciences
Southern Methodist University
Dallas, TX 75275

Dr. Indra Gupta
Teledyne Geotech
314 Montgomery Street
Alexandria, VA 22314

Prof. David G. Harkrider
Seismological Laboratory
Division of Geological & Planetary Sciences
California Institute of Technology
Pasadena, CA 91125

Prof. Donald V. Helmberger
Seismological Laboratory
Division of Geological & Planetary Sciences
California Institute of Technology
Pasadena, CA 91125

Prof. Eugene Herrin
Institute for the Study of Earth and Man
GeophysicalLaboratory
Southern Methodist University
Dallas, TX 75275

Prof . Robert B. Herrmann
Department of Earth & Atmospheric Sciences
St. Louis University
St. Louis, MO 63156

Prof. Bryan Isacks
Cornell University
Department of Geological Sciences
SNEE Hall
Ithaca, NY 14850

Dr. Rong-Song Jih
Teledyne Geotech
314 Montgomery Street
Alexandria, VA 22314

Prof. Lane R. Johnson
Seismographic Station
University of California
Berkeley, CA 94720

Prof. Alan Kafka
Department of Geology & Geophysics
Boston College
Chestnut Hill, MA 02167

Dr. Richard LaCoss
MIT-Lincoln Laboratory
M-200B
P. O. Box 73
Lexington, MA 02173-0073 (3 copies)

Prof Fred K. Lamb
University of Illinois at Urbana-Champaign
Department of Physics
1110 West Green Street
Urbana, IL 61801

Prof. Charles A. Langston
Geosciences Department
403 Deike Building
The Pennsylvania State University
University Park, PA 16802

Prof. Thorne Lay
Institute of Tectonics
Earth Science Board
University of California, Santa Cruz
Santa Cruz, CA 95064

Prof. Arthur Lerner-Lam
Lamont-Doherty Geological Observatory
of Columbia University
Palisades, NY 10964

Dr. Christopher Lynnes
Teledyne Geotech
314 Montgomery Street
Alexandria, VA 22314

Prof. Peter Malin
University of California at Santa Barbara
Institute for Crustal Studies
Santa Barbara, CA 93106

Dr. Randolph Martin, III
New England Research, Inc.
76 Olcott Drive
White River Junction, VT 05001

Dr. Gary McCartor
Mission Research Corporation
735 State Street
P.O. Drawer 719
Santa Barbara, CA 93102 (2 copies)

Prof. Thomas V. McEvilly
Seismographic Station
University of California
Berkeley, CA 94720

Dr. Keith L. McLaughlin
S-CUBED
A Division of Maxwell Laboratory
P.O. Box 1620
La Jolla, CA 92038-1620

Prof. William Menke
Lamont-Doherty Geological Observatory
of Columbia University
Palisades, NY 10964

Stephen Miller
SRI International
333 Ravenswood Avenue
Box AF 116
Menlo Park, CA 94025-3493

Prof. Bernard Minster
IGPP, A-025
Scripps Institute of Oceanography
University of California, San Diego
La Jolla, CA 92093

Prof. Brian J. Mitchell
Department of Earth & Atmospheric Sciences
St. Louis University
St. Louis, MO 63156

Mr. Jack Murphy
S-CUBED, A Division of Maxwell Laboratory
11800 Sunrise Valley Drive
Suite 1212
Reston, VA 22091 (2 copies)

Dr. Bao Nguyen
GL/LWH
Hanscom AFB, MA 01731-5000

Prof. John A. Orcutt
IGPP, A-025
Scripps Institute of Oceanography
University of California, San Diego
La Jolla, CA 92093

Prof. Keith Priestley
University of Cambridge
Bullard Labs, Dept. of Earth Sciences
Madingley Rise, Madingley Rd.
Cambridge CB3 OEZ, ENGLAND

Prof Paul G. Richards
L-210
Lawrence Livermore National Laboratory
Livermore, CA 94550

Dr. Wilmer Rivers
Teledyne Geotech
314 Montgomery Street
Alexandria, VA 22314

Prof. Charles G. Sammis
Center for Earth Sciences
University of Southern California
University Park
Los Angeles, CA 90089-0741

Prof. Christopher H. Scholz
Lamont-Doherty Geological Observatory
of Colun.bia University
Palisades, NY 10964

Thomas J. Sereno, Jr.
Science Application Int'l Corp.
10260 Campus Point Drive
San Diego, CA 92121

Prof. David G. Simpson
Lamont-Doherty Geological Observatory
of Columbia University
Palisades, NY 10964

Dr. Jeffrey Stevens
S-CUBED
A Division of Maxwell Laboratory
P.O. Box 1620
La Jolla, CA 92038-1620

Prof. Brian Stump
Institute for the Study of Earth & Man
Geophysical Laboratory
Southern Methodist University
Dallas, TX 75275

Prof. Jeremiah Sullivan
University of Illinois at Urbana-Champaign
Department of Physics
1110 West Green Street
Urbana, IL 61801

Prof. Clifford Thurber
University of Wisconsin-Madison
Department of Geology & Geophysics
1215 West Dayton Street
Madison, WS 53706

Prof. M. Nafi Toksoz
Earth Resources Lab
Massachusetts Institute of Technology
42 Carleton Street
Cambridge, MA 02142

Prof. John E. Vidale
University of California at Santa Cruz
Seismological Laboratory
Santa Cruz, CA 95064

Prof. Terry C. Wallace
Department of Geosciences
Building #77
University of Arizona
Tucson, AZ 85721

Dr. Raymond Willeman
GL/LWH
Hanscom AFB, MA 01731-5000

Dr. Lorraine Wolf
GL/LWH
Hanscom AFB, MA 01731-5000

OTHERS (United States)

Dr. Monem Abdel-Gawad
Rockwell International Science Center
1049 Camino Dos Rios
Thousand Oaks, CA 91360

Prof. Keiiti Aki
Center for Earth Sciences
University of Southern California
University Park
Los Angeles, CA 90089-0741

Prof. Shelton S. Alexander
Geosciences Department
403 Deike Building
The Pennsylvania State University
University Park, PA 16802

Dr. Kenneth Anderson
BBNSTC
Mail Stop 14/1B
Cambridge, MA 02238

Dr. Ralph Archuleta
Department of Geological Sciences
University of California at Santa Barbara
Santa Barbara, CA 93102

J. Barker
Department of Geological Sciences
State University of New York
at Binghamton
Vestal, NY 13901

Dr. T.J. Bennett
S-CUBED
A Division of Maxwell Laboratory
11800 Sunrise Valley Drive, Suite 1212
Reston, VA 22091

Mr. William J. Best
907 Westwood Drive
Vienna, VA 22180

Dr. N. Biswas
Geophysical Institute
University of Alaska
Fairbanks, AK 99701

Dr. G.A. Bollinger
Department of Geological Sciences
Virginia Polytechnical Institute
21044 Derring Hall
Blacksburg, VA 24061

Dr. Stephen Bratt
Center for Seismic Studies
1300 North 17th Street
Suite 1450
Arlington, VA 22209

Michael Browne
Teledyne Geotech
3401 Shiloh Road
Garland, TX 75041

Mr. Roy Burger
1221 Serry Road
Schenectady, NY 12309

Dr. Robert Burridge
Schlumberger-Doll Research Center
Old Quarry Road
Ridgefield, CT 06877

Dr. Jerry Carter
Rondout Associates
P.O. Box 224
Stone Ridge, NY 12484

Dr. W. Winston Chan
Teledyne Geotech
314 Montgomery Street
Alexandria, VA 22314-1581

Dr. Theodore Cherry
Science Horizons, Inc.
710 Encinitas Blvd., Suite 200
Encinitas, CA 92024 (2 copies)

Prof. Jon F. Claerbout
Department of Geophysics
Stanford University
Stanford, CA 94305

Prof. Robert W. Clayton
Seismological Laboratory
Division of Geological & Planetary Sciences
California Institute of Technology
Pasadena, CA 91125

Prof. F. A. Dahlen
Geological and Geophysical Sciences
Princeton University
Princeton, NJ 08544-0636

Prof. Adam Dziewonski
Hoffman Laboratory
Harvard University
20 Oxford St
Cambridge, MA 02138

Prof. John Ebel
Department of Geology & Geophysics
Boston College
Chestnut Hill, MA 02167

Eric Fielding
SNEE Hall
INSTOC
Cornell University
Ithaca, NY 14853

Prof. Donald Forsyth
Department of Geological Sciences
Brown University
Providence, RI 02912

Dr. Cliff Frolich
Institute of Geophysics
8701 North Mopac
Austin, TX 78759

Prof. Art Frankel
Mail Stop 922
Geological Survey
790 National Center
Reston, VA 22092

Dr. Anthony Gangi
Texas A&M University
Department of Geophysics
College Station, TX 77843

Dr. Freeman Gilbert
Inst. of Geophysics & Planetary Physics
University of California, San Diego
P.O. Box 109
La Jolla, CA 92037

Mr. Edward Giller
Pacific Sierra Research Corp.
1401 Wilson Boulevard
Arlington, VA 22209

Dr. Jeffrey W. Given
Sierra Geophysics
11255 Kirkland Way
Kirkland, WA 98033

Prof. Stephen Grand
University of Texas at Austin
Department of Geological Sciences
Austin, TX 78713-7909

Prof. Roy Greenfield
Geosciences Department
403 Deike Building
The Pennsylvania State University
University Park, PA 16802

Dan N. Hagedorn
Battelle
Pacific Northwest Laboratories
Battelle Boulevard
Richland, WA 99352

Kevin Hutchenson
Department of Earth Sciences
St Louis University
3507 Laclede
St. Louis, MO 63103

Prof. Thomas H. Jordan
Department of Earth, Atmospheric
and Planetary Sciences
Massachusetts Institute of Technology
Cambridge, MA 02139

Robert C. Kemerait
ENSCO, Inc.
445 Pineda Court
Melbourne, FL 32940

William Kikendall
Teledyne Geotech
3401 Shiloh Road
Garland, TX 75041

Prof. Leon Knopoff
University of California
Institute of Geophysics & Planetary Physics
Los Angeles, CA 90024

Prof. L. Timothy Long
School of Geophysical Sciences
Georgia Institute of Technology
Atlanta, GA 30332

Prof. Art McGarr
Mail Stop 977
Geological Survey
345 Middlefield Rd.
Menlo Park, CA 94025

Dr. George Mellman
Sierra Geophysics
11255 Kirkland Way
Kirkland, WA 98033

Prof. John Nabelek
College of Oceanography
Oregon State University
Corvallis, OR 97331

Prof. Geza Nagy
University of California, San Diego
Department of Ames, M.S. B-010
La Jolla, CA 92093

Prof. Amos Nur
Department of Geophysics
Stanford University
Stanford, CA 94305

Prof. Jack Oliver
Department of Geology
Cornell University
Ithaca, NY 14850

Prof. Robert Phinney
Geological & Geophysical Sciences
Princeton University
Princeton, NJ 08544-0636

Dr. Paul Pomeroy
Rondout Associates
P.O. Box 224
Stone Ridge, NY 12484

Dr. Jay Pulli
RADIX System, Inc.
2 Taft Court, Suite 203
Rockville, MD 20850

Dr. Norton Rimer
S-CUBED
A Division of Maxwell Laboratory
P.O. Box 1620
La Jolla, CA 92038-1620

Prof. Larry J. Ruff
Department of Geological Sciences
1006 C.C. Little Building
University of Michigan
Ann Arbor, MI 48109-1063

Dr. Richard Sailor
TASC Inc.
55 Walkers Brook Drive
Reading, MA 01867

John Sherwin
Teledyne Geotech
3401 Shiloh Road
Garland, TX 75041

Prof. Robert Smith
Department of Geophysics
University of Utah
1400 East 2nd South
Salt Lake City, UT 84112

Dr. Stewart Smith
IRIS Inc.
1616 North Fort Myer Drive
Suite 1440
Arlington, VA 22209

Dr. George Sutton
Rondout Associates
P.O. Box 224
Stone Ridge, NY 12484

Prof. L. Sykes
Lamont-Doherty Geological Observatory
of Columbia University
Palisades, NY 10964

Prof. Pradeep Talwani
Department of Geological Sciences
University of South Carolina
Columbia, SC 29208

Prof. Ta-liang Teng
Center for Earth Sciences
University of Southern California
University Park
Los Angeles, CA 90089-0741

Dr. R.B. Tittmann
Rockwell International Science Center
1049 Camino Dos Rios
P.O. Box 1085
Thousand Oaks, CA 91360

Dr. Gregory van der Vink
IRIS, Inc.
1616 North Fort Myer Drive
Suite 1440
Arlington, VA 22209

Professor Daniel Walker
University of Hawaii
Institute of Geophysics
Honolulu, HI 96822

William R. Walter
Seismological Laboratory
University of Nevada
Reno, NV 89557

Dr. Gregory Wojcik
Weidlinger Associates
4410 El Camino Real
Suite 110
Los Altos, CA 94022

Prof. John H. Woodhouse
Hoffman Laboratory
Harvard University
20 Oxford St.
Cambridge, MA 02138

Prof. Francis T. Wu
Department of Geological Sciences
State University of New York
at Binghamton
Vestal, NY 13901

Dr. Gregory B. Young
ENSCO, Inc.
5400 Port Royal Road
Springfield, VA 22151-2388

Dr. Ralph Alewine III
DARPA/NMRO
1400 Wilson Boulevard
Arlington, VA 22209-2308

Mr. James C. Battis
GL/LWH
Hanscom AFB, MA 01731-5000

Dr. Robert Blandford
DARPA/NMRO
1400 Wilson Boulevard
Arlington, VA 22209-2308

Eric Chael
Division 9241
Sandia Laboratory
Albuquerque, NM 87185

Dr. John J. Cipar
GL/LWH
Hanscom AFB, MA 01731-5000

Mr. Jeff Duncan
Office of Congressman Markey
2133 Rayburn House Bldg.
Washington, DC 20515

Dr. Jack Evernden
USGS - Earthquake Studies
345 Middlefield Road
Menlo Park, CA 94025

Art Frankel
USGS
922 National Center
Reston, VA 22092

Dr. T. Hanks
USGS
Nat'l Earthquake Research Center
345 Middlefield Road
Menlo Park, CA 94025

Dr. James Hannon
Lawrence Livermore Nat'l Laboratory
P.O. Box 808
Livermore, CA 94550

Paul Johnson
ESS-4, Mail Stop J979
Los Alamos National Laboratory
Los Alamos, NM 87545

Janet Johnston
GL/LWH
Hanscom AFB, MA 01731-5000

Dr. Katharine Kadinsky-Cade
GL/LWH
Hanscom AFB, MA 01731-5000

Ms. Ann Kerr
IGPP, A-025
Scripps Institute of Oceanography
University of California, San Diego
La Jolla, CA 92093

Dr. Max Koontz
US Dept of Energy/DP 5
Forrestal Building
1000 Independence Avenue
Washington, DC 20585

Dr. W.H.K. Lee
Office of Earthquakes, Volcanoes,
& Engineering
345 Middlefield Road
Menlo Park, CA 94025

Dr. William Leith
U.S. Geological Survey
Mail Stop 928
Reston, VA 22092

Dr. Richard Lewis
Director, Earthquake Engineering & Geophysics
U.S. Army Corps of Engineers
Box 631
Vicksburg, MS 39180

James F. Lewkowicz
GL/LWH
Hanscom AFB, MA 01731-5000

Mr. Alfred Lieberman
ACDA/VI-OA'State Department Bldg
Room 5726
320 - 21st Street, NW
Washington, DC 20451

Stephen Mangino
GL/LWH
Hanscom AFB, MA 01731-5000

Dr. Robert Masse
Box 25046, Mail Stop 967
Denver Federal Center
Denver, CO 80225

Art McGarr
U.S. Geological Survey, MS-977
345 Middlefield Road
Menlo Park, CA 94025

Richard Morrow
ACDA/VI, Room 5741
320 21st Street N.W
Washington, DC 20451

Dr. Keith K. Nakanishi
Lawrence Livermore National Laboratory
P.O. Box 808, L-205
Livermore, CA 94550

Dr. Carl Newton
Los Alamos National Laboratory
P.O. Box 1663
Mail Stop C335, Group ESS-3
Los Alamos, NM 87545

Dr. Kenneth H. Olsen
Los Alamos Scientific Laboratory
P.O. Box 1663
Mail Stop C335, Group ESS-3
Los Alamos, NM 87545

Howard J. Patton
Lawrence Livermore National Laboratory
P.O. Box 808, L-205
Livermore, CA 94550

Mr. Chris Paine
Office of Senator Kennedy
SR 315
United States Senate
Washington, DC 20510

Colonel Jerry J. Perrizo
AFOSR/NP, Building 410
Bolling AFB
Washington, DC 20332-6448

Dr. Frank F. Pilotte
HQ AFTAC/TT
Patrick AFB, FL 32925-6001

Katie Poley
CIA-OSWR/NED
Washington, DC 20505

Mr. Jack Rachlin
U.S. Geological Survey
Geology, Rm 3 C136
Mail Stop 928 National Center
Reston, VA 22092

Dr. Robert Reinke
WL/NTESG
Kirtland AFB, NM 87117-6008

Dr. Byron Ristvet
HQ DNA, Nevada Operations Office
Attn: NVCG
P.O. Box 98539
Las Vegas, NV 89193

Dr. George Rothe
HQ AFTAC/TGR
Patrick AFB, FL 32925-6001

Dr. Alan S. Ryall, Jr.
DARPA/NMRO
1400 Wilson Boulevard
Arlington, VA 22209-2308

Dr. Michael Shore
Defense Nuclear Agency/SPSS
6801 Telegraph Road
Alexandria, VA 22310

Dr. Albert Smith
Los Alamos National Laboratory
L-205
P. O. Box 808
Livermore, CA 94550

Donald L. Springer
Lawrence Livermore National Laboratory
L-205
P. O. Box 808
Livermore, CA 94550

Mr. Charles L. Taylor
GL/LWG
Hanscom AFB, MA 01731-5000

Mr. Steven R. Taylor
Lawrence Livermore National Laboratory
L-205
P. O. Box 808
Livermore, CA 94550

Dr. Eileen Vergino
Lawrence Livermore National Laboratory
L-205
P. O. Box 808
Livermore, CA 94550

Dr. Thomas Weaver
Los Alamos National Laboratory
P.O. Box 1663, Mail Stop C335
Los Alamos, NM 87545

J.J. Zucca
Lawrence Livermore National Laboratory
P. O. Box 808
Livermore, CA 94550

GL/SULL
Research Library
Hanscom AFB , MA 01731-5000 (2 copies)

Secretary of the Air Force
(SAFRD)
Washington, DC 20330

Office of the Secretary Defense
DDR & E
Washington, DC 20330

HQ DNA
Attn: Technical Library
Washington, DC 20305

DARPA/RMO/RETRIEVAL
1400 Wilson Boulevard
Arlington, VA 22209

DARPA/RMO/Security Office
1400 Wilson Boulevard
Arlington, VA 22209

Geophysics Laboratory
Attn: XO
Hanscom AFB, MA 01731-5000

Geophysics Laboratory
Attn: LW
Hanscom AFB, MA 01731-5000

DARPA/PM
1400 Wilson Boulevard
Arlington, VA 22209

Defense Technical Information Center
Cameron Station
Alexandria, VA 22314 (5 copies)

Defense Intelligence Agency
Directorate for Scientific
& Technical IntelligenceAttn: DT1B
Washington, DC 20340-6158

AFTAC/CA
(STINFO)
Patrick AFB, FL 32925-6001

TACTEC
Battelle Memorial Institute
505 King Avenue
Columbus, OH 43201 (Final Report Only)

Dr. Ramon Cabre, S.J.
Observatorio San Calixto
Casilla 5939
La Paz, Bolivia

Prof. Hans-Peter Harjes
Institute for Geophysik
Ruhr University/Bochum
P.O. Box 102148
4630 Bochum 1, FRG

Prof. Eystein Husebye
NTNF/NORSAR
P.O. Box 51
N-2007 Kjeller, NORWAY

Prof. Brian L.N. Kennett
Research School of Earth Sciences
Institute of Advanced Studies
G.P.O. Box 4
Canberra 2601, AUSTRALIA

Dr. Bernard Massinon
Societe Radiomana
27 rue Claude Bernard
75005 Paris, FRANCE (2 Copies)

Dr. Pierre Mecheler
Societe Radiomana
27 rue Claude Bernard
75005 Paris, FRANCE

Dr. Svein Mykkeltveit
NTNF/NORSAR
P.O. Box 51
N-2007 Kjeller, NORWAY

FOREIGN (Others)

Dr. Peter Basham
Earth Physics Branch
Geological Survey of Canada
1 Observatory Crescent
Ottawa, Ontario, CANADA K1A 0Y3

Dr. Eduard Berg
Institute of Geophysics
University of Hawaii
Honolulu, HI 96822

Dr. Michel Bouchon
I.R.I.G.M.-B.P. 68
38402 St. Martin D'Heres
Cedex, FRANCE

Dr. Hilmar Bungum
NTNF/NORSAR
P.O. Box 51
N-2007 Kjeller, NORWAY

Dr. Michel Campillo
Observatoire de Grenoble
I.R.I.G.M.-B.P. 53
38041 Grenoble, FRANCE

Dr. Kin Yip Chun
Geophysics Division
Physics Department
University of Toronto
Ontario, CANADA M5S 1A7

Dr. Alan Douglas
Ministry of Defense
Blacknest, Brimpton
Reading RG7-4RS, UNITED KINGDOM

Dr. Roger Hansen
NTNF/NORSAR
P.O. Box 51
N-2007 Kjeller, NORWAY

Dr. Manfred Henger
Federal Institute for Geosciences & Nat'l Res.
Postfach 510153
D-3000 Hanover 51, FRG

Ms. Eva Johannisson
Senior Research Officer
National Defense Research Inst.
P.O. Box 27322
S-102 54 Stockholm, SWEDEN

Dr. Fekadu Kebede
Seismological Section
Box 12019
S-750 Uppsala, SWEDEN

Dr. Tormod Kvaerna
NTNF/NORSAR
P.O. Box 51
N-2007 Kjeller, NORWAY

Dr. Peter Marshal
Procurement Executive
Ministry of Defense
Blacknest, Brimpton
Reading FG7-4RS, UNITED KINGDOM

Prof. Ari Ben-Menahem
Department of Applied Mathematics
Weizman Institute of Science
Rehovot, ISRAEL 951729

Dr. Robert North
Geophysics Division
Geological Survey of Canada
1 Observatory Crescent
Ottawa, Ontario, CANADA K1A 0Y3

Dr. Frode Ringdal
NTNF/NORSAR
P.O. Box 51
N-2007 Kjeller, NORWAY

Dr. Jorg Schlittenhardt
Federal Institute for Geosciences & Nat'l Res.
Postfach 510153
D-3000 Hannover 51, FEDERAL REPUBLIC OF GERMANY